Microscopic Imaging of Epigenetic Age.

Delany Rodriguez[1*], Martin Alvarez-Kuglen[1*], Haodong Qin[2*], Lorenzo Fiengo[1], Chen Farhy[1], Wei-Mien Hsu[3], Aaron Havas[1], Rozalyn M. Anderson[4], Amanda J. Roberts[5], Peter D. Adams[1], Tatyana O. Sharpee[3], and Alexey V. Terskikh[1#]
1. Sanford Burnham Prebys, La Jolla CA 92037.
2. University of California San Diego, La Jolla, CA 92093, USA
3. Salk Institute for Biological Studies, La Jolla, CA 92037, USA
4. University of Wisconsin, Madison, WI 53705, USA
5. The Scripps Research Institute, La Jolla, CA 92037, USA
* Equal contribution
# Correspondence: terskikh@sbp.edu

ABSTRACT.
Predictive biomarkers of functional or biological age are key for evaluating interventions aimed at increasing healthspan and, perhaps, lifespan in humans. Currently, cardiovascular performance, blood analytes, frailty indices, and DNA methylation clocks are used to provide such estimates; each technique has its own strength and limitations. We have developed a novel approach, microscopic imaging of epigenetic age (miEpiAge), which computes multiparametric signatures based on the patterns of epigenetic landscape in single nuclei. We demonstrated that such epigenetic age (EpiAge) readouts robustly distinguish young and old cells from multiple tissues and observed the emergency of epigenetic trajectories of aging using different embeddings of peripheral blood (e.g. CD3+ T cells) without linear regression or averaging. EpiAge readouts based on H3K4me1, H3K27ac, and H3K27me3 revealed distinct progression of epigenetic age in different tissues, while brain and heart were correlated (Spearman r=0.8, p=0.015), and suggested an overall slower pace of epigenetic changes in brain and kidney. Further, EpiAge readouts were consistent with expected acceleration or slowdown of biological age in chronologically identical mice treated with chemotherapy or following caloric restriction regimen, respectively. Critically, we demonstrated that miEpiAge readouts from mouse skeletal muscles correlate (Pearson r=0.92, p=5e-8) with linear combinations of circadian rhythms dependent whole organism metabolic and behavioral readouts recorded from the same mice. Because EpiAge readouts are derived from individual sample measurements without averaging or regression on chronological age, EpiAge represents a personalized biomarker. We posit that miEpiAge provides first in class approach to assess functional age in a variety of organs and tissues offering a rich collection of universal personalized biomarkers of functional age with a single cell resolution.

INTRODUCTION.
With a steady increase in average lifespan and population aging [1, 2], the need for biomarkers of functional age is pressing. Such biomarkers should perform better, compared to chronological age, to quantitate health risks and thus improve the effectiveness and quality of care in mid-life and old age while reducing associated cost [3-6].

Twelve interconnected distinctive features were proposed to drive aging [7]. One of them, epigenetic alterations, are likely to play a major role and the loss of epigenetic information was proposed to be a cause of mammalian aging [8]. Indeed, the advent of partial reprogramming provides a mounting evidence that transient expression of Yamanaka's OSKM factors [9] is sufficient for turning back the clock on at least some functional readouts of organs and tissues in old mice [10, 11].

Epigenetic changes during aging result in altered epigenome and chromatin accessibility, aberrant gene expression, reactivation of transposable elements, and genomic instability [12, 13]. Which specific epigenetic marks best convey age-dependent alterations is unclear, however, several studies linked aging to the loss of heterochromatin and alterations in global and local levels of H3K9me3, H3K27me3, H4K20me3, and H3K4me3 [14-16]. H3K9me3 marks constitutive heterochromatin [17]; H3K27me3, which is associated with promoters of repressed genes [18] and orchestrate development and differentiation [19]; H4K20me3, is associated with repression of transcription when present at promoters [18], is involved in silencing transposons [20], and controls cell senescence and tumors [21]; Deficiency in the H3K4me3 complex results in lifespan extension in worms [22]. The pattern of active enhancers, marked with a combination of H3K27ac & H3K4me1 [23], is also age-dependent [24, 25]. It is likely that information collectively encoded by the above epigenetic marks will be relevant to determine the progress of epigenetic and, perhaps, functional aging.

However, historically, fascinating serendipitous discoveries of Hannum [26] and Horvath [27] identified CpG sites in human blood and other tissues with age-dependent changes in DNA methylation enabling the development of epigenetic clocks (DNAmAge). Subsequently, multiple other combinations of CpGs / clocks have been established [28-31]. All DNA methylation clocks depend on linear regression (Elastic net regularization) algorithms or deep learning [32] to select CpGs whose average levels across hundreds to thousands samples fit best with chronological age (i.e. regression on chronological age). This approach produced excellent chronological clocks tailored to specific cell types or pan tissues [33].

The manifestations of aging vary dramatically among individuals of the same chronological age, bringing forth the notion of biological age which can be estimated using candidate biomarkers including cardiovascular performance, serum analytes, and deficit or frailty indices [6]. For DNAmAge the deviation from the average prediction of chronological age for everyone is considered a measure of biological age. One of the challenges of DNAmAge is separating the biological component from the chronological [33, 34]. PhenoAge [35] and GrimAge [30] clocks attempt to overcome this limitation through alternative training approaches by including additional CpGs regressed on empirically observed plasma proteins whose levels serve as surrogate biomarkers previously correlated with healthspan and lifespan. Critically, due to inevitable averaging (whether through linear regression or deep learning) to extract individual CpG weights, DNAmAge-based clocks will remain population level predictors rather than personalized instruments. Further, DNA methylation clocks are dependent on the particular method of calibration [36], often require large number of cells, and are not cost effective [33], underscoring the need for developing of alternative approaches to measure functional or biological age.

Several years ago, we developed microscopic imaging of epigenetic landscapes rooted in the analysis of epigenome topography in single nuclei of intact permeabilized cells [37]. We employed immunolabeling with antibodies specific for histone modifications (e.g. acetylation and methylation marks) and automated microscopy to capture patterns using image texture analysis, resulting in a multiparametric signatures of cellular states [37].

Here we took advantage of this technique to study aging and described a novel class of candidate biomarkers of functional aging based on microscopic imaging of epigenetic age (miEpiAge). Unexpectedly, we observed the emergency of epigenetic trajectories of aging without linear regression or averaging. EpiAge readouts revealed distinct progression of epigenetic age in different tissues and were consistent with expected acceleration or slowdown of biological age in chronologically identical mice treated with chemotherapy or following caloric restriction regimen, respectively. Critically, we demonstrated that miEpiAge readouts from mouse skeletal muscles correlate (Pearson r=0.92, p=5e-8) with linear combinations of circadian rhythms dependent

whole organism metabolic and behavioral readouts recorded from the same mice. We propose that miEpiAge provides first in class approach to assess functional age in a variety of organs and tissues offering a rich collection of universal personalized biomarkers of functional age with a single cell resolution.

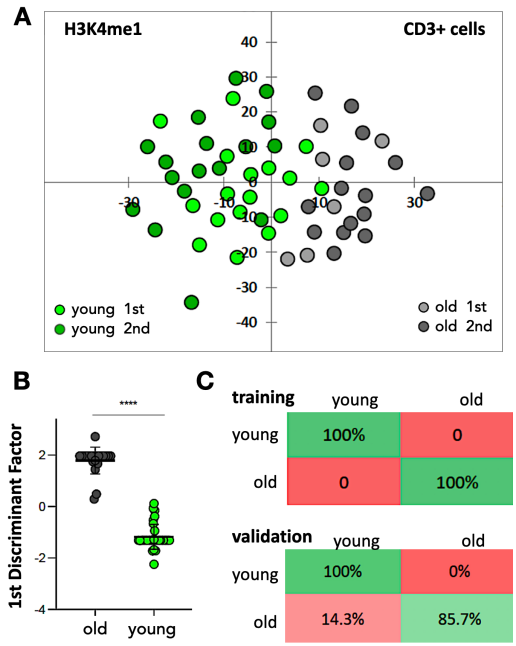

Fig. 1. Multiparametric signatures based on H3K4me1 mark (+DAPI) separates single CD3+ cells from young and old mice. (**A**) Multidimensional Scaling (MDS) plot of single CD3+ cells from 2 young and 2 old mice. (**B, C**) Quadratic discriminant analysis (QDA) using texture features derived from images obtained with anti-H3K4me1 + DAPI quantifies the separation between young vs old cell. (B) Scatter plot showing first discriminant factor (F1), **** $p<0.0001$ t-test; (C) confusion matrixes showing accuracy (percentage) of correct predictions for the training and validation sets.

RESULTS.

Multiparametric signatures distinguish young and old CD3+ subset of PBMC

We inquired whether multiparametric epigenetic signatures [37] could detect age-dependent epigenetic changes distinguishing cells from young and old mice. We first analyzed CD3+ subset of mouse PBMC immunolabeled with anti-H3K4me1and anti-CD3 (+DAPI) and multiparametric signatures were computed (see Materials and Methods for details). We observed a clear separation between young and old cells using multidimensional scaling (MDS) algorithm implemented in XLSTAT software (**Fig. 1A**). Further, individual CD3+ cells from young and old mice were readily discriminated with 85.7% accuracy using quadratic discriminant analysis (QDA) (**Fig. 1B, C**). These results suggest that multiparametric signatures of epigenetic landscape in single cells are sufficient to distinguish young and old CD3+ cells with high accuracy.

Multiparametric signatures discriminate young vs old freshly isolated cells of different types.

Based on availability and ease of harvesting we focused on freshly isolated hepatocytes and splenocytes from 5 months or 25 months old C57BL/6J males. Hepatocytes were purified via a 2-step perfusion method modified from [38] resulting in ~98% pure viable primary hepatocytes. Cells were fixed, immunolabeled (separately) with anti-H3K9me3, anti-H3K27me3, or anti-H4K20me3 (+DAPI), and multiparametric signatures were computed. We discovered that multiparametric signatures based on any of the above epigenetic mark robustly (92-100% accuracy) discriminated between young and old hepatocytes as well as young and old splenocytes (**Supplementary Fig. 1A, B**). Further, we analyzed de-identified "young" (18-28 years old) and "old" (53-62 years old) normal human peripheral blood mononuclear cells (PBMC) obtained from a commercial source. We discovered a robust (96-100% accuracy) separation between the young and the old primary human PBMC (**Supplementary Fig. 1C**). These results suggest that multiparametric epigenetic signatures based on well-characterized epigenetic marks of heterochromatin can discriminate between young and old freshly isolated mouse and human cells.

Linear regression of multiparametric epigenetic signatures provides excellent chronological clock.

Next, we inquired whether multiparametric epigenetic signatures could be regressed onto chronological age. We obtained mouse PBMC ranging from 53 to 968 days from C57BL/6J males using classical Ficoll centrifugation procedure. Cells were fixed, immunolabelled with anti-H3K4me1 and anti-CD3 to focus on T cell subset of PBMC and multiparametric signatures were computed. We employed classical linear regression analysis implemented in XLSTAT package (Base, v19.06) to select features with the best prediction power/correlation

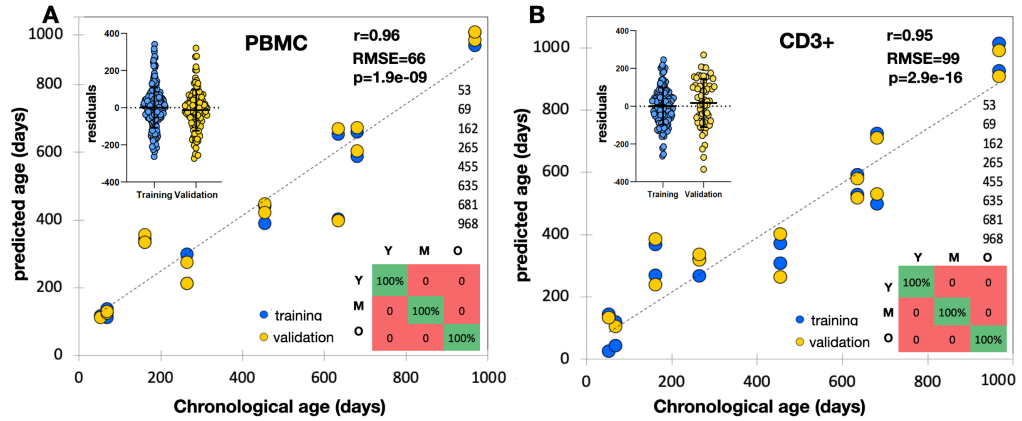

Fig. 2. Linearly regressed multiparametric epigenetic signatures correlate with chronological age. Dot plots of linear regression analysis for training and validation sets using PBMC or CD3 T cell subset multiparametric signatures based on H3K4me1 (+DAPI). Each dot is individual animal. Inserts in the left top corner, residuals distribution using 10 technical replicates per each mouse to better visualize the distribution. Insert in the right lower corner, quadratic discriminant analyses confusion matrix based on the validation set accurately (100%) separates signatures of young (Y) vs middle age (M) vs old (M) PBMC and CD3+ T cells.). r, Person correlation coefficient. RMSE, root mean square error, p, statistical significance of Pearson correlation. Regression trendline is shown for the validation set.

with chronological age. We observed an excellent (r=0.96, RMSE= 66, p=1.9e-9 for the validation set) correlation of the regressed features with chronological age (**Fig. 2A**). The residuals were normally distributed and centered similarly to the training set, validating an assumption a normal distribution. To avoid the artifacts of cellularity change with age (e.g. increased myeloid and decreased lymphoid representation) we have analyzed only the CD3+ cells representing a total T cell compartment. Similar to that observed for PBMC, we detected a very good (r=0.95, RMSE=99, p=2.9e-16 for the validation set) correlation of the regressed features with chronological age for the CD3+ cells (**Fig. 2B**). Quadratic discriminant analysis using linear regression-adjusted signatures of young (53-69 days), middle age (162-455 days), and old (632-968 days) mice separated all three groups with 100% accuracy for both PBMC and CD3+ T cells. These results argue for the utility of H4K20me3-based epigenetic signatures to measure chronological age in mouse PBMC and CD3+ T cells. Given the power of MIEL to discriminate between other types of young and old cells including human PBMC, we predict the utility of chronological EpiAge for many other cell types of mice and men.

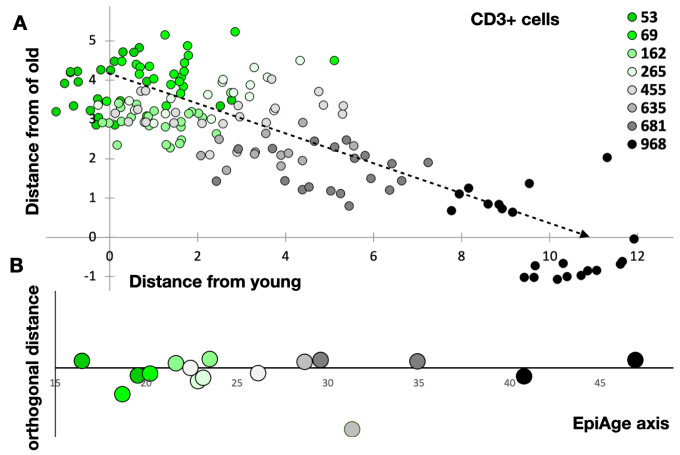

Fig. 3. Defining EpiAge axis for CD3+ subset of PBMCs. (**A, B**) Dot plots of the epigenetic distance from the centroids of youngest mice (53 days, X axis) and the distance from the centroids of oldest mice (968 days, Y axis). Each point is a technical replicate (well mean, n=12 / mouse, ~3000 cells / replicate). Mouse ages (days) are color coded. Dotted line connecting the centroids of the oldest mice to the centroids of the youngest mice visualizing the EpiAge axis.

Aging trajectories of epigenetic signatures support the notion of epigenetic age (EpiAge) axis.

Next, we investigated the trajectories of epigenetic signatures with respect to age without the assumption of linear progression or trajectory and without applying linear regression (or any other feature transformation) of the texture features space. To that end we computed the coordinates of centroids of all datapoints from youngest and oldest mice in the multidimensional space. Subsequently we computed the distances from each datapoint (all ages) to the centroids of the youngest and oldest mice enabling us to plot each datapoint in such coordinates (**Fig. 3A**). We observed a distribution of data points from

youngest to oldest mice around the respective centroids with intermediate aged datapoints falling in-between the youngest and oldest mice for both CD3+ cells and PBMCs (**Fig. 3A and Supplementary Fig. 2A**)

These results suggested an apparent age-related progression of epigenetic signatures along a linear trajectory between the youngest and the oldest mice. Therefore, we designed a new axis connecting the centroids of the youngest and oldest mice signatures hereon referred to as the "EpiAge axis." The progression of each replicate was evaluated by projecting onto the EpiAge axis. In addition, we considered distance perpendicular EpiAge axis as "orthogonal distance" axis (**Fig. 3B , Supplementary Fig. 2A**). Note that all distances and projections should be first computed in the multidimensional Euclidean space and the results are then plotted in 2D space as EpiAge vs orthogonal distance. The EpiAge axis now provides a simple readout of the proximity to the oldest / youngest centroids and the orthogonal axis estimates the deviation from the "perfect" epigenetic age trajectory along EpiAge axis. Note, that the position of each mouse on EpiAge axis is a mere projection of its entire multiparametric signature without linear regression or any other manipulations.

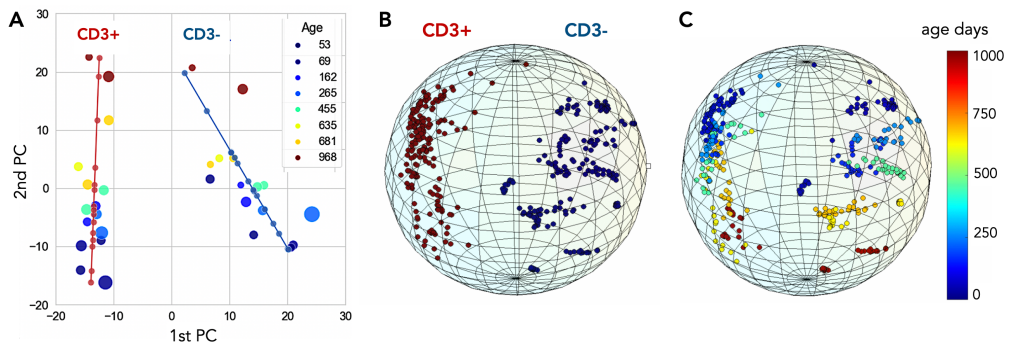

Fig. 4. Alternative analysis of age-dependent progression of epigenetic signatures. **A.** Euclidian PCA separates datapoint by cell type CD3+ vs CD3- (PC1) and separation of datapoints within each lineage by age (PC2). Each dot is a centroid of a mouse. **B.** A 3-dimantrional hyperbolic embedding separates CD3+ and CD3- subsets of PBMC. Each dot is a technical replicate (well mean, n=12 / mouse, ~3000 cells / replicate) **C.** Same 3-dimentional hyperbolic embedding as in (B), but the datapoints are colored by age to reveal the emergence of the aging trajectories. Movies of B and C are available upon request.

Alternative computational techniques extract intrinsic aging trajectories

To pressure test the emerging age-related progression of epigenetic signatures projected on the EpiAge axis, we employed a straightforward Principal Component Analysis (PCA). We compared complimentary subpopulations of PBMC, namely CD3+ and CD3- cells. PCA revealed a clear separation of datapoint by cell type CD3+ vs CD3- (mainly by PC1) and progression of age-related multiparametric signatures within each lineage (mainly by PC2) (**Fig. 4A**). Note that axis of the age separation in CD3+ population is nearly parallel to PC2, hence, in this case PC2 is similar to the EpiAge axis for CD3+ cells.

Further, to explore yet another alternative route of analysis we took advantage of the Hyperbolic space recently proven to be particularly helpful to analyze complex biological datasets [39-42]. We embedded CD3+ and CD3- cell distance matrix into a 3-dimensional hyperbolic space with (Poincare ball) curvature = -25.0 (dimensionality and curvature were optimized as previously described [39, 40] (also see Materials and Methods). We observed a clear separation of epigenetic signatures between CD3+ and CD3- cells in a 3-dimensional hyperbolic space (**Fig. 4B**) as well as the emergence of age-related progression of multiparametric signatures for both CD3+ and CD3- subsets of PBMCs (**Fig. 4C**). In sum, the concordant results obtained by three independent computational approaches strongly suggest the presence of intrinsic aging trajectories within epigenetic signatures of mouse PBMCs and CD3+/- subsets. Note that none of the methods described above employs averaging of individual organism readouts, linear regression on chronological age, or any

other manipulation of texture feature values to reveal the intrinsic progression of multiparametric signatures along the aging axis (i.e. from the youngest samples to the oldest samples).

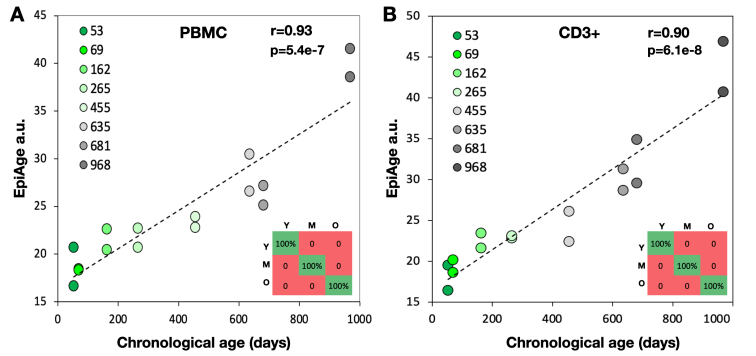

Fig. 5. EpiAge readouts correlate with chronological age. Dot plot of EpiAge readouts vs chronological age. Native multiparametric signatures based on H3K4me1 (+DAPI) were used without linear regression. Each dot is individual animals. Insert in the right lower corner, quadratic discriminant analyses confusion matrix based on the validation set accurately (100%) separates signatures of young (Y) vs middle age (M) vs old (M) PBMC and CD3+ T cells.). r, Person correlation coefficient. RMSE, root mean square error, p, statistical significance. Trendline is shown for visualization purposes only.

EpiAge correlates with chronological age

Intrigued by an intrinsic age-associated progression of epigenic EpiAge readouts we plotted EpiAge readouts vs chronological age. Remarkably, we observe a rather good (r=0.93, PBMC and r=0.90, CD3+ cells) correlation with chronological age (**Fig. 5**), albeit lower compared to the model based on linear regression. Similar to that observed for the linear regression model, quadratic discriminant analysis using unmanipulated multiparametric signatures of young (53-69 days), middle age (162-455 days), and old (632-968 days) mice separated all three groups with 100% accuracy for both PBMC and CD3+ T cell. The limited numbers of mice (16 total) precluded us from obtaining more refined statistics.

Comparative analysis of EpiAge trajectories in 5 solid organs

Recent studies suggested that organs and tissues may age at different pace in the same organism [43, 44]. To directly compare EpiAge trajectories in different organs and tissues, we developed a protocol to isolate nuclei from flash-frozen solid tissues and perform the analysis of epigenetic landscape similar to that described for the freshly fixed cells (see Materials and Methods). We investigated the distribution of EpiAge readouts in 5 major organs including brain, heart, kidney, liver, and skeletal muscles (quadriceps) in 3 cohorts of mice, young (2 months), middle age (15 months) and old (27 months). We employed antibodies specific for H3K27me3, H3K27ac, H3K4me1 (+DAPI) to computed multiparametric signatures as previously described [37] (**Supplementary Figure 3**).

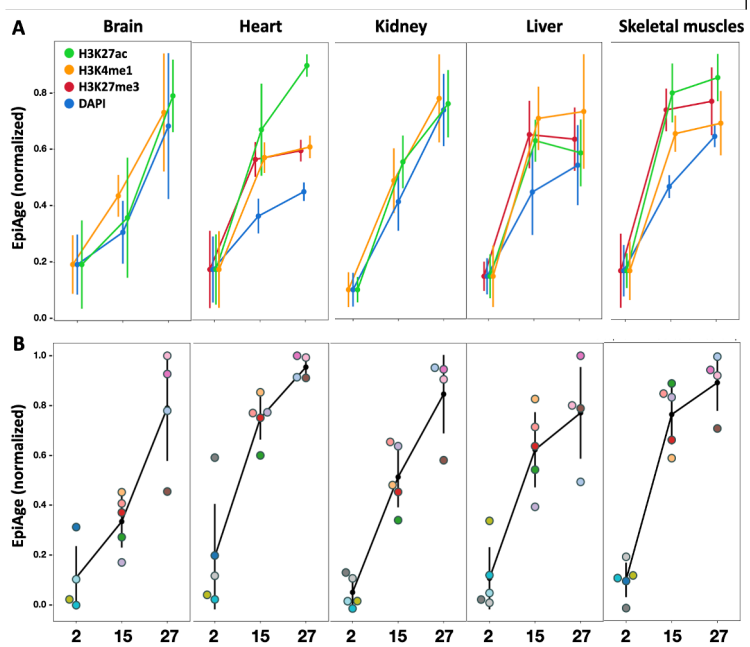

Fig. 6. Comparative analysis of EpiAge trajectories in brain, heart, kidney, liver, and skeletal muscles. A. Normalized progression for individual epigenetic marks (+DAPI). **B.** Normalized progression for combined EpiAge. Individual mice are color coded. Standard deviations for each age group.

The EpiAge values from 2- and 27-months animals was normalized (0 to 1) for all marks and tissues to enable comparative analyses including the progress of the middle age (15-months) mice along EpiAge axis. We observed that EpiAge was increased on average with chronological age in all tissues and organs analyzed (**Fig. 6**). We observed similar EpiAge trajectories for all epigenetic marks tested in brain and

kidney, whereas the pace of age-dependent changes in heart, liver and skeletal muscles diverged depending on the mark with the changes in basic chromatin manifold (revealed by DAPI) occurred at the slowest rate (**Fig. 6A**). We observed a slower age-related progression of epigenetic aging (all marks combined EpiAge) in the brain as compared to all other tissues ($p<0.001$, one way ANOVA, with Tukey post hoc test). Notably, this observation parallels a previously observed deceleration of DNAmAge in the brain compared to other organs and tissues [45, 46] suggesting a concordance between the two approached based on distinct epigenetic marks (i.e. DNA methylation and histone modifications). Given that 5 organs for which EpiAge was analyzed came from the same mice, we were able to compare the relative pace of EpiAge progression between these 5 organs. The only robust and significant correlation observed was between brain and heart (Spearman's $r=0.8$, $p=0.015$) suggesting that the pace of functional aging in these organs may correlate. Indeed, some evidence for the brain – heart aging connection, both in mice and in humans, exist in the literature [47-49].

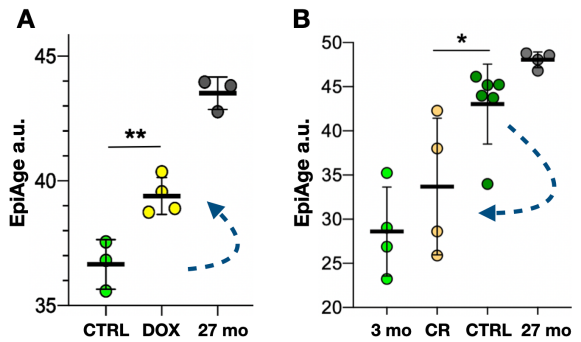

Fig. 7. EpiAge detects epigenetic alterations induced by DOX and CR. Dot plot comparing EpiAge readouts based on H3K27me3 + H3K27ac marks (+DAPI) of **A.** liver hepatocytes isolated from untreated 3 months controls (CTRL), DOX-treated mice (DOX), and old mice (27 months) **B.** liver nuclei isolated from 3 months and 27 months age controls, CR mice (5 months 25% CR), an diet control mice (CTRL). *=$p<0.05$, **=$p<0.001$, one-way ANOVA with Tukey's post hoc.

EpiAge distinguishes experimental perturbation affecting biological age

Previous work from the Campisi laboratory [50] and others [51-53] demonstrated the age-accelerating effect of widely used chemotherapeutic agents. We followed Demaria et al., 2017 [50] protocol for DOX treatment (10 mg/kg, i.p.; controls received PBS). Live hepatocytes were isolated 21 days post injection using a 2-step perfusion method modified from [38] resulting in ~98% pure viable primary hepatocytes. Day 21 post DOX treatment was chosen to focus on aging-related changes as opposed to acute response to DNA damage and stress response. Purified hepatocytes were plated in 384 well plates, fixed, immunolabelled with anti-H3K9me3 and anti-H3K27ac (+DAPI), imaged, multiparametric signatures were computed as before [37] and projected onto EpiAge axis as described above. We observed that DOX treatment shifted the EpiAge readouts from freshly isolated liver hepatocytes towards that of an older age (**Fig. 7A**).

Multiple studies suggest that caloric restriction (CR) increase healthspan and slows down the aging process in diverse species [54-56]. We employed frozen liver samples from control C57BL/6 and CR mice restricted (25% between 2 and 7 months). Nuclei were purified from frozen liver tissues as previously described [57], distributed in 384 well plates, fixed, and immunolabelled with anti-H3K9me3 and anti-H3K27ac (+DAPI). Images and multiparametric epigenetic signatures were acquired as before [37] and projected onto EpiAge axis as described above. We observe that CR treatment on average shifts the EpiAge readouts in liver hepatocytes towards that of a younger age (**Fig. 7B**). These observations suggest that EpiAge readouts in liver hepatocytes on average track with experimental perturbation of biological age.

EpiAge in skeletal muscles correlates with linear combination of whole organism functional readouts

Next, we inquired whether multiparametric epigenetic signatures could be associated with the whole organism functions. Namely, we conducted metabolic, cognitive, and motor behavioral tests in chronologically identical C57BLACK/6 males (experimental mice age=25 months, N=18) and acquire epigenetic signatures from the same mice. We employed Comprehensive Lab Animal Monitoring System (CLAM) which includes measurements of rearing, ambulation, sleep, food, water, oxygen consumption, and CO_2 release throughout

24 hours. Cognitive tests included Bernes mase, novel object recognition, open field, novel object recognition, and nest building. Motor tests included measurements of gait, grip strength, hanging wire, treadmill, and rotarod performances. We used young (2 months, N=5) and old (27 months, N=5) mice as age and biological references to derive epigenetic signatures of chronologically and biologically distinct young and old mice. For epigenetic signatures we focused on skeletal muscles (quadriceps), which bear functional load of motor behavior, and mediate systemic metabolism [58]. Nuclei were isolated from flash frozen tissues, immunolabeled with H3K27ac + H3K27me3 antibodies (+DAPI), imaged, and multiparametric epigenetic signatures were acquired as previously described [37].

First, we computed the information distance matrix using epigenetic signatures from the reference (young and old) and experimental mice in Euclidean space as previously described [59] (also see Materials and Methods). Next, we embedded such information distance matrix into a 3-dimensional hyperbolic space with curvature = -18.0 (dimensionality and curvature were optimized as previously described [39, 40] (also see Materials and Methods).

To visualize data in the hyperbolic space we use hyperbolic Poincare ball, which is one of the models that defines a manifold with hyperbolic geometry. The 3-dimentional hyperbolic embedding was used for the purpose of visualization (**Fig. 8A, B**). The shortest distance between two points in the hyperbolic space is no longer a straight line, but a curved line called geodesic. We took advantage of the logarithmic and exponential representations, which map the points from the hyperbolic Poincare ball to the tangent space centered at a reference point and vice versa [60]. The tangent space is Euclidean, and the curved geodesic in the hyperbolic space can be approximated by a straight line in the tangent space enabling us to find the best fitted geodesic in the hyperbolic space through finding the best fitted straight line in the tangent space.

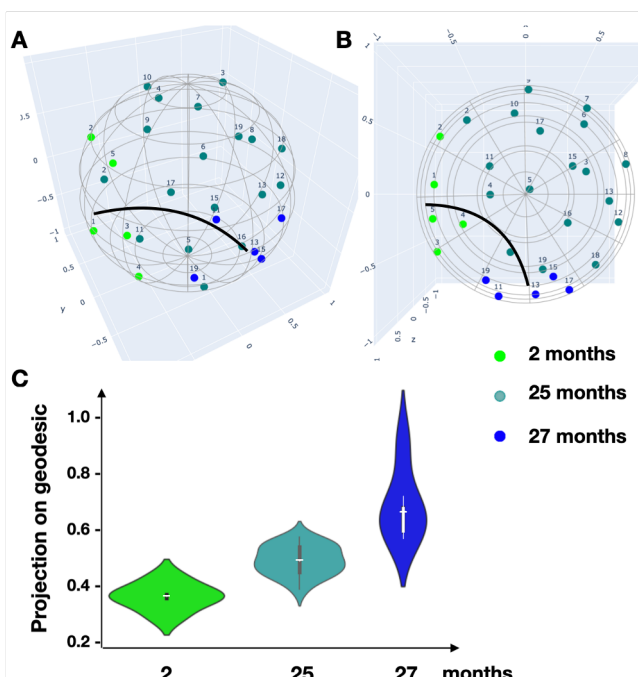

Fig. 8. Visualization of hyperbolic embedding. A-B. Two different views of the information distance matrix embedded into a 3-dimentional hyperbolic space. The black curve is a geodesic connecting the centers of young and old mice in the hyperbolic space **C.** Violin plots of the projections on geodesic (i.e. EpiAge distribution on geodesic) for young (2 months) old (27 months) and experimental (25 months) mice.

We computed the geodesic between the centroids of young and old reference mice in the hyperopic space and projected coordinates of all mice (young old, experimental) onto this geodesic generating the distribution of EpiAge measurements. As seen for other tissues (in both Euclidian and Hyperbolic spaces), we observed a robust separation between the EpiAge from young and old reference mice and the EpiAge of experimental mice were distributed in-between the EpiAge of reference mice (**Fig. 8C**)

Next, we inquired whether EpiAge correlated with individual readouts of metabolic parameters, cognitive, or motor behaviors. With the exception of average sleep (Pearson r=-0.6, p=0.08), we observed no significant correlations, perhaps underscoring the complexity of EpiAge and biological age phenotype. Instead, we took

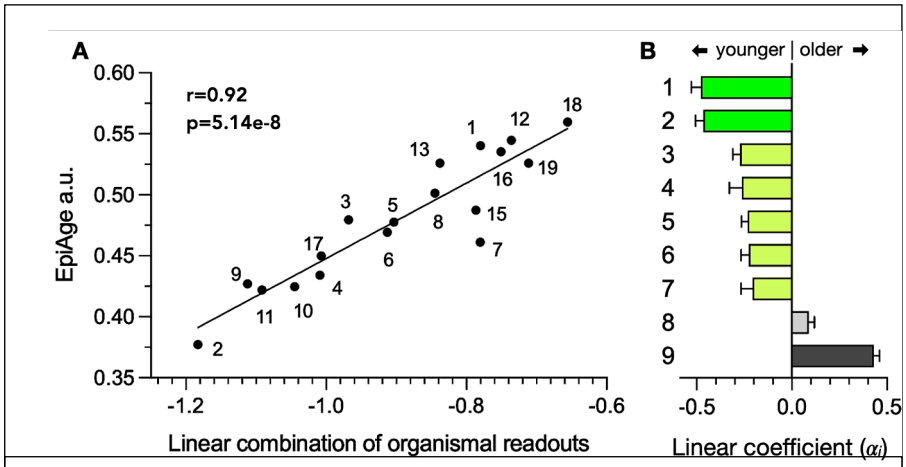

Fig. 9. EpiAge of skeletal muscles correlates with linear combination of metabolic and behavioral whole organism readouts. A. Correlation between EpiAge ($\vec{t}$, projection on geodesic) and the linear combination (effect on EpiAge on top) of metabolic and behavioral readouts ($\sum_i \alpha_i \vec{f_i}$). **B.** Linear coefficients α_i for 9 orthogonal clusters encompassing colinear primary readouts $\vec{f_i}$ listed in Table 1. Readouts in each cluster has the same weight (same linear coefficient α_i).

advantage of a combinatorial approach. Assume that we have n samples with different biological age as a columns vector of dimension n, $\vec{t}$, and N behavior feature with each feature is also a column vector of dimension n as $\vec{f_i}$ where i is an index for the feature between 1 and N. Instead of calculating the correlation between the EpiAge $\vec{t}$ and each individual readout $\vec{f_i}$, we can analyze the collective contribution of readouts to EpiAge by examining the correlation R between the EpiAge $\vec{t}$ and the optimal linear combination of features $\sum_i \alpha_i \vec{f_i}$, where$\{\alpha_i\}$ is the set of coefficients that maximize $|r|$, minimize the p value, and $\sum_i \alpha_i^2 = 1$.

Highly variable non-significant features were removed. To ensure the uniqueness of the linear coefficients α_i, we computed the correlation matrix between all normalized significant feature vectors (i.e. correlation between individual behaviors, **Supplementary Fig. 4**) and grouped together the feature vectors $\vec{f_i}$ which are correlated with each other into orthogonal clusters.

Table.1 Orthogonal clusters of whole organism readouts.

#	Organismal readouts
1	Rearing difference (night-day)
1	Average Rearing night
2	Average sleep
3	Open field distance moved
3	Open field velocity
3	Open field time in center
4	Average Activity night
4	Activity difference (night-day)
4	Average ambulation night
4	Ambulation difference (night-day)
5	Gait consistency
6	Barnes maze activity
7	Average O2 night
7	Average O2 day
7	Average CO2 night
7	Average CO2 day
8	O2 difference (night-day)
8	CO2 difference (night-day)
9	Average Rearing day
9	Average ambulation day

We identified 9 major orthogonal cluster of behavioral readouts and used a representative individual readout $\vec{f_i}$ from each cluster to compute linear coefficients for each cluster. We conducted 4 trials of jackknife for F_i to sample the variance for each feature, and 1000 trials to sample the variance for the combinatorial process to maximize the correlation and to obtain the distribution of linear coefficients α_i for each cluster $\vec{f_i}$. The linear combination of the 9 orthogonal clusters of metabolic and behavioral readouts provided excellent (Pearson r=0.92 p=5.14e-8), correlation with EpiAge (**Fig. 9A**). Such nearly perfect and highly significant correlation of EpiAge with relatively small number of whole organism metabolic and behavioral readouts underscores potential utility of EpiAge as a single biomarker of functional or biological age in skeletal muscles and, possibly, other tissues and organs.

The linear coefficient α_i is proportional to the contribution, positive or negative, of each cluster to EpiAge. Because individual readouts $\vec{f_i}$ are normalized and colinear within each cluster, we consider each of individual readouts within the cluster contribute to EpiAge with the same coefficient α_i. Such computations enabled us to identify key metabolic readouts and behaviors with positive or negative contribution to EpiAge (**Fig. 9B, Table 1**). Remarkably, adherence to circadian rhythms was the overarching motif for the contribution of individual behavioral and metabolic readouts to EpiAge. All forms of activity during the night (the active phase for nocturnal animal) were associated with a reduction of EpiAge whereas the same

activity during the day (the inactive / sleep phase for nocturnal animal), was associated with an increase of EpiAge. Sleep was universally associated with reduction of EpiAge. Rearing, including its differential (night-day), was identified as the most salient contributor EpiAge. Curiously, quadriceps (skeletal muscles tissues used to obtain epigenetic signatures) are the main muscle involved in the rearing action. Day time ambulation and rearing were colinear salient components contributing to increase of EpiAge. Readouts of open field and Barnes maze activities and gait consistency (recorded during the night) were associated with reduction of EpiAge. Several metabolic measurements such as average O_2 and CO_2 volumes were associated with a reduction of EpiAge, while their night-day differential was associated with increase of EpiAge collectively suggesting that adherence to circadian cycles or lack thereof exerts the major effect on EpiAge.

Taken together, our findings suggest that EpiAge may be a single integrator of a number of functional readouts and suggest a utility of EpiAge beyond a simple correlation with chronological age. Our findings also point to the most salient functions, locomotor activity, sleep, oxygen volume, and gait and the importance of circadian rhythms to integrate these functions. EpiAge readouts are derived from individual sample measurements without averaging or regression on chronological age thus representing personalized biomarkers of functional age with a single cell resolution.

DISCUSSION.

Biomarkers of aging are key to facilitate effective health control in the rapidly aging population in US and worldwide to quantitate health risks and to improve the effectiveness and quality of care in mid-life and old age while reducing associated cost. Major type of such biomarker (and biological age calculators) developed include standard physiological measurements and molecular markers (based on DNA, RNA, proteins, metabolites, etc.). Individually, these markers are not informative in part because their levels could simply manifest an age-associated pathology, for instance acute inflammation, rather than indicate functional or biological age. Combinatorically, these markers are effective estimators in large study cohorts; however, they vary significantly at the individual level [61]. Indeed, whether based on simple linear regression or Elastic net regularization (such as DNA methylation clocks PhenoAge [35], GrimAge [30], and meta-clock [45]) or deep learning approaches to classify human behavior for biological age prediction [62], current biological clocks average individual readouts and regress thousands of individual measurements on chronological age then calling the deviation from average a measure of individual biological age.

One of our most surprising findings is the discovery of intrinsic aging trajectories within multiparametric epigenetic signatures that could be rendered and visualized using both Euclidian and hyperbolic metrics. Remarkably, miEpiAge approach does not require linear regression or any other manipulation of hundreds of multiparametric texture features to extract the age-related progression of multiparametric signatures along the aging trajectory. Instead EpiAge measurements rely on distance matrix computations in different geometry and embeddings. We take it as a hint that unmanipulated multiparametric signatures may provide better estimation of biological differences between the animals. Our observations suggest the presence of an intrinsic age-related order in the multidimensional space of texture features, perhaps reflecting the robust spatial organization of 3-dimensional epigenetic landscapes in single nuclei and its evolution with age. It will be informative to further elucidate the structure of the feature space and the relationships between texture features obtained from imaging different epigenetic marks. Further, it would be revealing to compare the aging trajectories obtained from multiparametric signatures of different epigenetic marks and their combinations to determine the individual marks trajectories of age-related changes. Indeed, each individual may have a series of biological ages, depending on the biomarker, suggesting that the biological ageing process may not just vary between individuals, but also within each individual [63]. The availability of specific and sustainable

antibodies to dozens of epigenetic marks as well as large volume of computations are likely to be the major limitations moving in that direction.

The aging process is associated with functional interconnected decline across multiple organs therefore impacting the health of the entire organism; the decline of one organ can promote the dysfunction of the entire organism accelerating the aging process [64]. However, several studies suggested that organs and tissues within the same organism could age at a different rate and identified diverse set of aging profiles termed ageotypes [44, 65, 66]. Transcriptomic analysis in mice has demonstrated that organs show an inter- and intra-organ progression of aging [67]. Perhaps not surprisingly, the most common differentially expressed genes across organs were related to immune response [67, 68].

Although EpiAge increased on average with chronological age in all tissues and organs analyzed, we observed a slower age-related progression of epigenetic aging in the brain as compared to all other tissues. Indeed, such deceleration of epigenetic aging in the brain compared to other organs and tissues was previously observed using DNA methylation clocks [45, 46]. Curiously, the progression of all 3 epigenetic marks and DAPI was the most concordant in the brain among all tissues analyzed. This result suggests that brain age-dependent epigenetic changes (both histone modifications and DNA methylation) proceeds at a slower pace compared to other tissues. Our data also suggests that all histone modification marks (as well as DAPI which labels chromatin manifold) change in synch, perhaps reflecting the importance of balanced cell function preservation in the brain. We observed significant correlation of EpiAge readouts between brain and heart (Spearman's $r=0.8$, $p=0.015$) suggesting these organs may have common determinants of epigenetic aging. Notably, a significant increase in super oxide radical production was seen in mitochondria prepared from the brain and the heart (but not in other organs) as rats aged [47]. Damage to mitochondria DNA in Ames dwarf mice, was significantly lower (~30%) in their brain and heart (but not in other organs) compared to the wild type controls [48]. Finally, cardiac index was associate with brain aging in the Framingham Heart Study [49]. In fact, decreased cardiac function, even at normal cardiac index levels, was associated with accelerated brain aging [49]. Taken together these studies point to potential correlates of age-related metabolic changes in brain and heart.

It appears that different cancers and cancer treatments induce epigenetic changes therefore increasing genome instability and accelerating the pace of organismal aging [69-73]. In particular, DNA damage (especially at a high rate) is known to induce cancer and accelerate aging [74-76] suggesting that, paradoxically, chemotherapy while suppressing an actively growing tumor, may promote delayed onset of neoplastic transformations. Most chemotherapy treatments have damaging effects to the entire organism and accelerate the aging process [50, 77-79]. It has been noted that cancer survivors develop age-related conditions faster (compared to healthy people) including increased frailty, chronic organ dysfunction, increase of cardiovascular diseases, cognitive impairment and secondary cancers [52, 80-83]. We observed a shift of EpiAge readouts towards that of the old animals in mice treated with Doxorubicin, resembling the observations in humans [53]. It will be important to investigate whether EpiAge readouts could faithfully report the effects of other chemotherapy drugs, evaluate different doses, regimens, and duration of treatment in various tissues. Quantitating the age acceleration following chemotherapy may help fine tuning and tailoring chemo regimens, quantify the utility of proposed dietary approaches that increase the resilience to chemotherapy [84], and possibly design new interventions aimed to reduce or eliminate accelerated aging following chemotherapy.

Because CR robustly increases maximum lifespan and delays biological aging in diverse scenarios [54-56], albeit the full picture could be more complex [85, 86]. successfully applied CR regimens help understanding the biology of aging [87-89] and could help recovery after chemotherapy in clinic [84]. We have observed a shift

in EpiAge readouts in CR animals towards that of young animals consistent with the phenotypic observations. It will be important to further refine these analyses, covering different CR regimens in mice and other species (e.g. monkeys), and to correlate the epigenetic changes with functional readouts at the organismal level as well as with various OMICs datasets (e.g. gene expression, chromatin accessibility, and enrichment for various epigenetic marks).

Remarkably, we observed a uniform alignment of metabolic and behavioral measurements contributing to EpiAge with circadian rhythms. Indeed, adherence to circadian rhythms appears to be the most critical unifying biological phenomena promoting both healthspan and lifespan. Circadian rhythms deteriorate with age [90] and age-dependent alterations in circadian rhythms dysregulate gene expression in the human cortex [91] and precipitate the loss of neural function [92]. Alterations in the regulation of circadian rhythms contribute to number of conditions for which the risk is increased in old age (e.g., sleep disturbances, dementia, and depression) [93]. In fact, average sleep was one of the strongest contributors to reduced EpiAge independent from the locomotor activity at night. Lack of sleep has been linked to accelerated aging in Drosophila [94] sleep duration in middle and old age with incidence of dementia [95] and sleep duration and age-related changes in brain structure and cognitive performance [96]. Fuhrer, mouse models lacking circadian clock components exhibit reduced life expectancy likely may be due to their inability to properly control and synchronize energy expenditure [97-99]. Circadian clock and biological clock could be physiologically linked through the endocrine rhythms and metabolic cycle [100]. Taken together the association of universal fabric of circadian rhythms with virtually all redouts contributing to EpiAge testifies for the biological relevance of EpiAge readouts.

The largest group of behaviors that correlated with EpiAge, always in a circadian-dependent fashion, comprised various flavors of locomotor activity. Age-related decline in locomotor activity is universal feature of living organism well documented in Drosophila [101] and insects in general [102], rodents [103], dogs [104], primates [105], and humans [106] where it is associated with cognitive impairment and decline in brain dopamine activity [107]. Curiously, rearing (and to a lesser degree ambulation) appeared to be the most salient activity contributing to EpiAge in a circadian-dependent manner. Rearing is a stereotyped behavior that appears to be stable within a given animal and provides a robust estimate of individual exploratory activity or reduced anxiety [108]. Rearing activity is an exploratory behavior of rodents related to information gathering or cognitive behavior [109]. Locomotion and rearing are very reliable factors for exploratory behavior in mice [110, 111]. It remains to be clarified whether the prominent contribution of rearing to EpiAge is related to the fact that we used quadriceps, which bear the bulk of rearing efforts, as skeletal muscle tissue to obtain EpiAge readouts.

While rearing and ambulation (and their differentials between night and day) were obtain from CLAM recordings (see materials and methods), other readouts of activity, such as open field distance moved, open field velocity, open field time in center (likely to be the consequence of the generalized activity), Barnes maze activity, and gait coordination, were obtained through conventional behavior test, however, conducted during the night time (for mice). These behaviors contributed to the reduced EpiAge thus confirming the universal respect of circadian dependency for behavioral contribution to EpiAge.

We observed that measurements of O2 and CO2 volume contributed to the reduced EpiAge. Indeed, oxygen consumption in untrained C57BL/6J mice (resting VO2, average VO2, and VO2max) declined with age [112] and expanded healthspan and lifespan in Myc heterozygous mice is associated with increased oxygen consumption irrespective of day/night [113] making the these metrics logical readout of younger metabolism. However, O2 and CO2 volume difference between night and day contributed to the increased EpiAge, which

dovetails with the observation that oxygen consumption during the nighttime is relatively higher in old mice compared to the young mice [113], making the night-day difference a plausible indicator of mouse aging.

Individually, most clinical biomarkers are insufficiently sensitive to measure the pace of aging and biological age. Studies, however, have shown that certain combinations of biomarkers are more reliable predictors of biological age or mortality [114]. Given robust correlation of EpiAge with key physiological, behavioral, and metabolic metrics underlying functional decline with age (and not the metrics of overt pathologies such as cancer, neurodegeneration, cardiovascular disfunction) we posit that EpiAge could be used as a single and personalized biomarker of functional age. This rather audacious hypothesis could be experimentally tested by determining whether EpiAge could provide predictive value, for instance, by longitudinal sampling of a given tissues (blood or solid tissue biopsy) from the same organism and measuring the function performance of that given tissues with age and upon intervention.

The exact nature of epigenetic structures constituting a functional substrate of EpiAge measurements remains to be identified. The nature of current statistical features (threshold adjacency statistics) makes it difficult to assign biological significance to an individual feature. Different approaches are undertaken including ones that explore colocalization of multiple epigenetic marks. We speculate that EpiAge could be related to the function of epigenetic maintenance system to preserve tissue and organ specific chromatin and epigenetic information. The information theory of aging propose that aging in eukaryotes is due to the loss of transcriptional networks and epigenetic information over time possibly due to the relocalization of chromatin modifiers [115, 116]. Indeed, information distance metrics coupled with Hyperbolic embedding provided the most informative insights into functional relevance of EpiAge readouts.

Since their discovery almost a decade ago, DNA methylation clocks have gained major grounds and have been widely explored in different areas of biological and medical studies [44-46]. However, the intrinsic reliance on averaging across large cohorts (simple linear regression or Elastic net regularization on chronological age) represents a limitation for DNAmAge use as a personalized predictive biomarker [3, 117, 118]. It will be informative to directly compare and contrast DNA methylation clocks with miEpiAge. Whereas we anticipate an overall concordance of the two approaches, the differences are likely to emerge based on the underlying methodologies. The DNA methylation clocks have high DNA region-specific resolution capable of pinpointing the exact locations of selected CpGs islands. Although individual CpGs usually don't significantly correlate with age, collectively, their enrichment in particular areas of genome (e.g. enhancer regions [47]) may inform on the molecular mechanisms of underlying age-related changes. Detecting the exact chromatin regions responsible for any given multiparametric signature of the imaged nuclei will be challenging. However, miEpiAge could be more sensitive to functional differences at the individual tissue, organ, and organism level due to the single cell resolution thus serving as personalized biomarker of epigenetic age. Several DNAm clocks (PhenoAge [22], GrimAge [16], meta-clock [48]) were trained to track with multiple age-associated pathologies. It will be important to explore whether EpiAge readouts could faithfully detect different age-associated disease states and conditions. Because the response to any intervention varies and is highly individual, it will be most important to determine whether EpiAge can provide a truly personalized biomarker that can predict the efficacy of an intervention for each individual.

LIMITATIONS OF THIS STUDY.

The current study has several limitations. The cellular composition of PBMC is changing with age and the frequency of CD3+ T cell subtypes (e.g. proportions of circulating naïve vs memory T cells) is changing as well, and this change in cellularity could be a confounding factor. We have examined only a limited number of

epigenetic marks and have not yet addressed their combinatorial complexity, which is the key feature of chromatin architecture. The 2-dimentional maximum projections of a 3-dimentional nuclei inevitably degrade the information content, stressing the need to develop 3-dimentional approaches to volume texture analysis. In addition, known variability and vulnerability related to isolating the intact unperturbed nucelli from flash frozen tissues could affect our results.

MATERIALS AND METHODS.

Mice

Experiments were conducted according to guidelines and protocols approved by the Institutional Animal Care and Use Committee (IACUC) of Sanford Burnham Prebys Medical Discovery Institute. Data presented within this manuscript were obtained using male mice. C57BL/6 mice, ranging in age from 2 to 27 months old, and were obtained from National Institute on Aging, Aged Rodent Colonies (RRID:SCR_007317).

Mouse behavioral studies.

EchoMRI testing. The EchoMRI 3-in-1 instrument (EchoMRI LLC, Houston, TX) is a quantitative nuclear magnetic resonance (qNMR) imaging system for whole body composition analysis of unaesthesized small animals [119, 120], and qNMR body composition analysis with EchoMRI instrumentation has been proposed to be "gold standard" methodology for metabolic studies in the mouse [121]. Following calibration, each mouse was put in a holder and placed into the EchoMRI chamber and lean mass, fat mass and water mass was calculated.

Optomotor test. The optomotor allows for assessment of visual ability and consists of a stationary elevated platform surrounded by a drum with black and white striped walls. Each mouse is placed on the platform to habituate for 1 minute and then the drum rotates at 2rpm in one direction for 1 minute, is stopped for 30 sec, and then rotates in the other direction for 1 minute. The number of head tracks (15 degree movements at speed of drum) is recorded. Blind mice do not track the moving stripes.

Comprehensive Laboratory Animal Monitoring System (CLAMS). Indirect calorimetry was performed in acclimated, singly-housed mice using a computer-controlled, open-circuit system (Oxymax System) that is part of an integrated Comprehensive Lab Animal Monitoring System (CLAMS; Columbus Instruments, Columbus, OH: [122, 123]). Testing occurred in clear respiratory chambers (20 × 10 × 12.5 cm) equipped with a sipper tube delivering water, food tray connected to a balance, and 16 photobeams situated in rows at 0.5 in intervals to detect motor activity along the *x*- and *z*-axes. Room air is passed through chambers at a flow rate of 0.5 L/min. Exhaust air from each chamber is sampled at 15-min intervals for 1 min. Sample air is sequentially passed through O_2 and CO_2 sensors (Columbus Instruments) for determination of O_2 and CO_2 content, from which measures of oxygen consumption (VO_2) and carbon dioxide production (VCO_2) are estimated. Outdoor air reference values are sampled after every 8 measurements. Gas sensors are calibrated prior to the onset of experiments with primary gas standards containing known concentrations of O_2, CO_2, and N_2 (Airgas Puritan Medical, Ontario, CA). Respiratory exchange ratios (RER) were calculated as the ratio of carbon dioxide production (VCO_2) to oxygen consumption (VO_2). Energy expenditure measures (VO_2, VCO_2 and heat formation [(3.815 + 1.232*RER)*VO_2 (in liters)]) were corrected for effective metabolic mass by using each mouse's lean mass obtained from the EchoMRI test.

Open field test. This test predicts how animals respond when introduced into a brightly illuminated open arena [124]. It is a classical test of "emotionality" used to measure anxiety-like responses of rodents exposed to stressful environmental stimuli (brightly illuminated open spaces) as well as to capture spontaneous activity measures. The

apparatus is a square white Plexiglas (50 x 50 cm) open field illuminated to 600 lux in the center. Each animal is placed in the center of the field and several behavioral parameters (distance traveled, velocity, center time, frequency in center) are recorded during a 5-minute observation period and analyzed using Noldus Ethovision XT software.

Novel object recognition test. This test assays recognition memory while leaving the spatial location of the objects intact and is believed to involve the hippocampus, perirhinal cortex, and raphe nuclei [125-127]. The basic principal is that animals explore novel environments and that with repeated exposure decreased exploration ensues (i.e., habituation; [128]). A subsequent object substitution results in dishabituation of the previously habituated exploratory behavior ([128-130]) and is expressed as a preferential exploration of the novel object relative to familiar features in the environment. Mice were individually habituated to a 51cm x 51cm x 39cm open field for 5 min. They were then be tested with two identical objects placed in the field for 5 min. After two such trials (each separated by 1 minute in a holding cage), the mouse was tested in the object novelty recognition test in which a novel object replaced one of the familiar objects. Behavior was video recorded and then scored for object contact time. The first time the mice were tested the objects used were clear plastic rectangular boxes filled with blue marbles and green plastic drink bottles filled with water and for the second test the objects were amber glass bottles and glass flasks filled with beige marbles. All objects were too tall for the mice to climb up on and too heavy for the mice to move.

Footprint Pattern Test. Basic gait measures can be assessed using simple footprint pattern analysis [131, 132]. Non-toxic paint was applied to each mouse's paws (a different color was used for front and back paws). The mouse was then placed at one end of a runway covered in paper and allowed to ambulate until their paws no longer left marks. Measurements were forelimb and hindlimb stride lengths (left and right) and front and back leg stride widths. Three full strides were averaged for each mouse's values. Data were excluded from mice that did not make 3 measurable strides (i.e. they circled or stopped).

Barnes maze test. This is a spatial memory test [133-135] sensitive to impaired hippocampal function [136]. Mice learn to find an escape chamber (19 x 8 x 7 cm) below one of twenty holes (5 cm diameter, 5 cm from perimeter) below an elevated brightly lit and noisy platform (75 cm diameter, elevated 58 cm above floor) using cues placed around the room. Spatial learning and memory were assessed across 4 trials (maximum time is 3 min) and then directly analyzed on the final (5th) probe trial in which the tunnel was removed and the time spent in each quadrant was determined, and the percent time spent in the target quadrant (the one originally containing the escape box) was compared with the average percent time in the other three quadrants. This is a direct test of spatial memory as there is no potential for local cues to be used in the mouse's behavioral decision.

Grip strength test. Grip strength was measured with a mouse Grip Strength Meter (Columbus Instruments) according to the manufacturer's instructions (User Manual 0167-007). All-limb measurements were performed with the angled grid attachment, pulling the mouse towards the meter by the tail after engagement of all limbs. Four consecutive measurements per mouse were taken and the highest three values were averaged, and data were expressed as newtons of peak force.

Hanging wire test. The hanging wire test allows for the assessment of grip strength and motor coordination [137, 138]. Mice were held so that only their forelimbs contact an elevated metal bar (2 mm diameter, 45 cm long, 37 cm above the floor) held parallel to the table by a large ring stand and let go to hang. Each mouse was given three trials separated by 30 seconds. Each trial was scored as follows and the average for each mouse was calculated: 0 — fell off, 1 — hung onto the wire by two forepaws, 2 — hung onto the wire by two forepaws, but also attempted to climb onto the wire, 3 — hung onto the wire by two forepaws plus one or both hindpaws around the wire, 4 — hung onto the wire by all four paws plus tail wrapped, 5 — escaped (crawled to the ring stand and righted itself or climbed down the stand to the table). Latency to falling off was also measured up to a maximum of 30 s.

Rotarod test. Rotarod balancing requires a variety of proprioceptive, vestibular, and fine-tuned motor abilities as well as motor learning capabilities [132]. An Accurotar rotarod apparatus (Omnitech Electronics, Inc.,

Columbus, OH) was used in these studies. A protocol was used whereby the rod starts in a stationary state and then begins to rotate with a constant acceleration of 10 rpm. When the mice were incapable of staying on the moving rod, they fell 38cm into a sanichip bedding filled chamber, breaking a photobeam in the process. The time of fall (translated to the speed at fall) was recorded by computer. The mice were tested in four sets of 3 trials, alternating directions between sets which were 30 min apart.

Treadmill test. The treadmill exhaustion test evaluates exercise capacity and endurance [139]. Mice are motivated to run to exhaustion in order to escape a shock at the base of the treadmill. Mice were trained to run in three daily 5 min sessions in which stopping would result in the mice touching the back of the apparatus and experiencing a mild shock (200 msec pulses of electric current with pulse repetition rate of 3 times per second (3 Hz) and an intensity of 1 mA). The treadmill speed for training was 10 m/min (0.373 mph). For the exhaustion test, the speed was initially set at 10 m/min for 5 min, and was increased 2 m/min every 2 min up to a maximum speed of 46 m/min (1.7 mph). The mice were run until they were exhausted or the maximal speed was achieved (which would mean a maximum run time of 41 min). Exhaustion was defined as the inability of the animal to run on the treadmill for 10 sec despite receiving shocks, a maximum of 30 mild shocks. To prevent injury, the mice were monitored carefully and continually during each session, and immediately upon meeting the criterion for exhaustion the shock grid was turned off and the mouse was removed from the treadmill.

Isolating Nuclei from Frozen Tissues

Flash-frozen in liquid nitrogen (stored at -80°C) is a common practice to preserve tissue and organs that are not to be processed immediately [140-142]. Organs and tissues were collected from freshly dissected mice, snap frozen using liquid Nitrogen, and stored at – 80°C. Organs and tissues were then transferred to a pre-chilled mortar and laid on top of dry ice; liquid Nitrogen was poured over the frozen tissue and a pestle was used to grind and pulverized the sample until a uniformly fine powder was obtained. Pulverized sample was the aliquoted and returned to – 80°C. To extract nuclei from frozen aliquots, 500 ul homogenization buffer (Nuclear Isolation Buffer 1 (NIM1) consisting of 250 mM Sucrose, 25 mM KCL, 10 mM Tris-buffer pH 8.0, 5 mM $MgCl_2$, 1 mM DTT, and 10% Triton X-100) were added to powdered tissue and transferred to the mixture a glass Dounce homogenizer and dounced ~ 10 times (avoiding bubbles) on ice. Add homogenization buffer up to 1 mL and filter homogenization solution through a 40 mm cell strainer. Centrifuge filtered solution at 600xg (acceleration 4, deacceleration 4) for 4 min at 4° C. Aspirate supernatant and resuspend in 200 mL of PBS. Nuclei were then count on CellDrop FL (DeNovix) using 1:1 Acridine Orange /Propidium Iodide and homogenization solution. Samples were diluted in PBS to 1 million/mL to seed each well (~30,000 cells in 30 mL/well) of 384 well plate (Perking Elmer PhenoPlate 384-well black, clear flat bottom Cat No. 6057300) pre-coated (1 mL/25 cm^2) with poly-L-Lysine (50 mL/mg). Centrifuge plate at 4000xg for 15 min at 4° C and immediately added 60 mL of 4% PFA to each well and incubate for 15 min at 4° C. Followed by one wash of PBS then proceed with MIEL.

Isolating Peripheral Blood Mononuclear Cells (PBMC's)

200 mL of blood was collected retroorbital for each mouse and immediately mixed with an equal volume of 50 mM EDTA (to prevent coagulation). Blood mixture was further diluted with 200 mL of PBS and carefully layering on top of 750 mL of Ficoll-Paque Plus (Millipore Sigma Cat. No. GE17-1440-02); followed by density gradient centrifugation at 700xg for 30 minutes at room temperature. The PBMC rich layer (cloudy phase) was carefully collected avoiding mixing the above and below layers and transferred to a new tube containing 10 mL of PBS. The PBMC mixture was centrifuged at 700xg for 20 minutes at room temperature and then removed supernatant and resuspend pellet in 1 mL of PBS. Isolated PBMC's were counted manually using a hemocytometer (Hausser Scientific Cat. No. 3120). Samples were diluted in PBS to 1 million/mL to seed each well (~30,000 cells in 30 mL/well) of 384 well plate (Perking Elmer PhenoPlate 384-well black, clear flat bottom Cat No. 6057300) pre-coated (1 mL/25 cm^2) with poly-L-Lysine (50 mL/mg). Centrifuge plate at 4000xg for 15

min at 4° C and immediately added 60 mL of 4% PFA to each well and incubate for 15 min at 4° C followed by PBS wash.

Imaging of Epigenetic Landscapes

Wells were blocked with 2% BSA in PBS 0.5% Triton X-100 for 1 hour at room temperature, and then incubated with primary antibody overnight at 4C and then washed with PBS 3x (5 minutes each at room temperature). Next, wells were incubated with secondary antibody overnight at 4C and then washed with PBS 3x (5 minutes each at room temperature). Antibodies were used at the following concentrations: Anti H3K27ac 1:1000 (Active Motif Cat No. 39685), and /or Anti H3K27me3 1:1000 (Active Motif Cat No. 39155), and/or Anti H3K4me1 1:1000 (Active Motif Cat No. 61633). Antibodies were detected using the following secondary antibodies for their appropriate hots: Goat anti-Rabbit IgG (H+L) Alexa Fluor™ 488 (Thermo Fisher Scientific Cat. No. A11034), and Donkey anti-Mouse IgG (H+L) Alexa Fluor™ 488 (Thermo Fisher Scientific Cat. No. A31570). Wells were counterstained with DAPI (Thermo Fisher Scientific Cat. No. D1306) during the secondary antibody staining and plates were sealed with adhesive foil (VWR Cat. No. 60941-124). Cells/nuclei were imaged on either an Opera Phenix high-content screening system (PerkinElmer) or an IC200-KIC (Vala Sciences) using a 20x objective. At least five fields/well and a total of 9 z-stacks at a 1mm z-step for Opera Phenix and nine fields/well and a total of 10 z-stacks at a 1mm z-step for IC200 were acquired and five wells per mouse sample were imaged. Unless stated otherwise, at least three wells and a minimum of 300 cells for each condition were used for analysis.

Image Segmentation, Feature Extraction and Analysis

We employed either commercial Acapella 2.6 (PerkinElmer) software package or a custom build python script, which was benchmarked against Acapella software performance. Briefly, DAPI images were used to segment out nuclei generating segmentation masks and object details using either Acapella or StarDist (Schmidt et al, 2018) within a custom python script. Segmentation masks were applied to all channels to isolate raw images of each nucleus in each channel. Size thresholds were then applied to isolate nuclei from debris. Texture features (Threshold Adjacency Statistics) were calculated from each nucleus for each channel as previously described [24]. Either WellMean statistics or bins of 200 nuclei (randomly sampled without replacement per experimental condition) were used to compute value for each feature for the mean sample (data point) statistics. All features were first normalized via z-scoring. PCA, MDS, or UMAP were calculated from the feature-statistics using the full feature set. Pairwise Euclidean distances were calculated from the feature-statistics. Directionless distance matrix was calculated per data point by averaging the Euclidean distance of that data point to each data point in the reference group. EpiAge distance was calculated as previously described [24].

Multidimensional scaling (MDS) and Discriminant Analysis

The Euclidean distances between all texture feature vectors were calculated to assemble a dissimilarity matrix (size N, where N is the number of populations being compared). For representation, the N matrix was reduced to a Nx2 matrix with MDS using the Excel add-on XLSTAT (Base, v19.06), and visualized as a 2D scatter plot. Quadratic discriminant analysis was conducted using the Excel add-on XLSTAT (Base, v19.06). The model was generated in a stepwise (forward) approach using default parameters. All features derived from images of tested histone modification were used for analysis following normalization by z-score. Features displaying multicollinearity were reduced. Model training was done as previously described [37].

Doxorubicin treatment

Two months old C57BL/6 mice were intraperitoneal injected with doxorubicin (Santa Cruz Biotechnology, Cat. No. 25316-40-9) 10 mg/Kg. Doxorubicin was diluted in 150mM NaCl solution, and control mice were injected

only with the vehicle solution (150mM NaCl). Fourteen days after treatment, mice were sacrificed and liver collected and immediately snap frozen in liquid nitrogen.

Caloric Restriction studies

Animal studies were conducted in accordance with approved protocols submitted through the respective Institutional Animal Care and Use Committees (IACUCs) at the University of Wisconsin Madison. Caloric Restriction mice: male C57BL/6N mice were individually housed under pathogen free conditions. Mice were randomized into control or restricted groups at 2 months of age and fed the AIN-93M semi-purified diet (Bio-Serv) either a Control diet (95% ad libitum) or Restricted diet (25% less than control). The mice were sacrificed at 7 months of age and tissues were harvested, flash frozen and stored at -80°C.

Information distance metric

We have used a distance metric based on the mutual information. Considering two random variables X and Y that are normalized between 0 and 1, the mutual information $I(X,Y)$ measures how much uncertainty of one variable is reduced by knowing the other variable. In other words, $I(X,Y)$ measures the uncertainty that mutually existed in both variables. The variation of information $D(X,Y)$ [59], or information distance metric we call here, is a measure of uncertainty of either variable by knowing the other variable. The information distance can be written in terms of marginal entropies: $H(X)$, $H(Y)$, and joint entropy $H(X,Y)$

$D(X,Y) = \frac{H(X,Y)-I(X,Y)}{H(X,Y)} = \frac{2H(X,Y)-H(X)-H(Y)}{H(X,Y)}$	(1)

In practice, we can consider two samples as X and Y, with corresponding feature values x_i and y_i where $1 \leq i \leq N_{feature}$ and $N_{feature}$ is the number of features. We can use construct a distribution of $P(z_0)$ and $P(z_1)$ based on the number density of x_i and y_i using histogram, where z_0, z_1 are the centers of the bin in the histogram. The entropy can be calculated using the Shannon entropy $H(z) = -\sum_{z \in Z} p(z) \log(p(z))$ for $z = z_0, z_1$.

Hyperbolic embedding

Hyperbolic geometry provides continuous approximation to tree-like hierarchical system, resulting in the distinguishing property of exponential expansion of states compared to quadratic expansion of states in the Euclidean space [143]. The hyperbolic geometry can be visualized using Poincare half space model and Poincare disk [143]. Hyperbolic space is better suited compared to Euclidean space for representing complex multipara metrical biological datasets. This is because hyperbolic space enables using fewer dimensions, inferring the hidden nodes based on the activity of observed "leaf" nodes, and reading out the "centrality" of each node [144-146]. Considering the aging process is due to a sequence of biological changes, and each change is chosen from a variety of choices, hence the number of possible states increase exponentially. We employed the Hyperbolic Multidimensional Scaling (HMDS) [42], which is a version of MDS in the hyperbolic space. Euclidean MDS minimize the difference between the distances calculated in the original Euclidean data space and the distances calculated in the high dimensional reduced space. Once we specify the dimension of the reduced space, the quality of embedding could be assessed using Shepherd diagram, which compares the distance in the original space and the distance in the dimensionality reduced hyperbolic space.

ACKNOWLEDGEMENTS

We greatly appreciate invaluable help of Sanford Burnham Prebys animal and high throughput imaging core facilities personnel and leadership in particular Mary O'Rourke-Braxtan and Susanne Heynen-Genel. We thank Collin Kaufman for much help with preparing tissues samples. We thank Kenta Ninomiya and all members of the Terskikh laboratory for helpful discussion. This work was supported by NIH grants R21 AG068913 and R21 AG075483 to A.V.T.

AUTHOR CONTRIBUTIONS

S.A.S., R.C.L., and A.V.T. designed and supervised the study; S.A.S., P.C., and A.C. conducted the experiments and structural modeling; S.A.S., P.C., R.C.L, and A.V.T. analyzed the data and prepared the manuscript.

COMPETING FINANCIAL INTERESTS

The authors declare no competing financial interests.

SUPPLEMENTARY FIGURES.

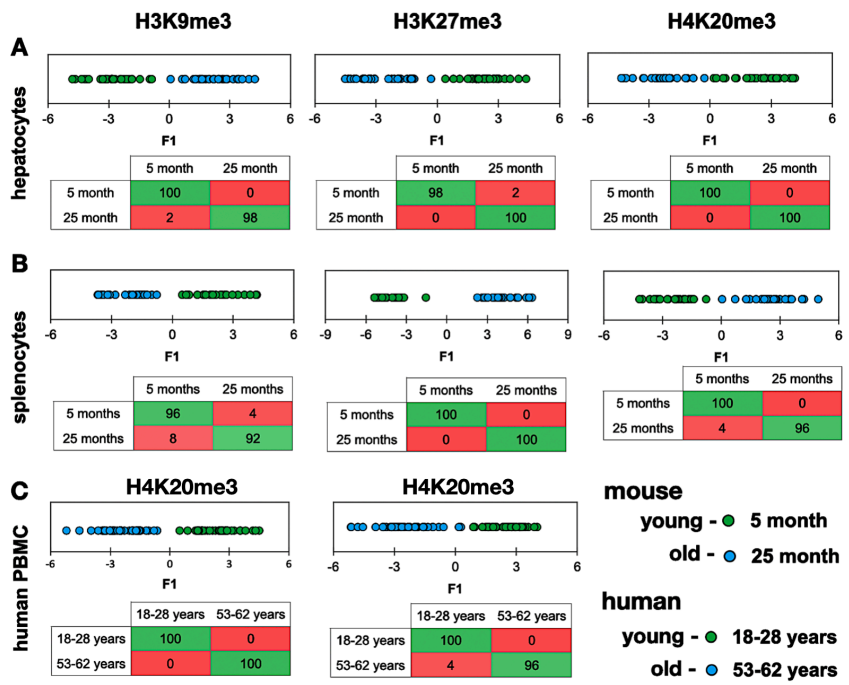

Supplementary Figure 1. Quadratic discrimination analysis using freshly isolated cells. Quadratic discriminant analysis using texture features derived from images obtained using antibodies to H3K9me3, H3K27me3, H4K20me3 (columns) was used to separate (**A**) mouse hepatocytes (**B**) mouse splenocytes, (**C**) human PBMC. Top rows, scatter plot showing first discriminant factor (F1), lower rows, confusion matrixes showing accuracy (percentage) of correct predictions for the validation set; larger numbers (and green color coding) suggest better prediction.

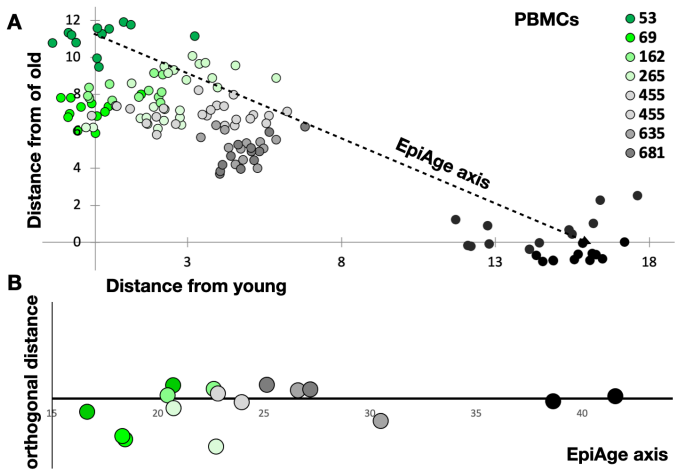

Supplementary Figure 2. EpiAge axis for total PBMCs. (A, B) Dot plots of the epigenetic distance from the centroids of youngest mice (53 days, X axis) and the distance from the centroids of oldest mice (968 days, Y axis). Each point is a technical replicate (well mean, n=12 / mouse, ~3000 cells / replicate). Mouse ages (days) are color coded. Dotted line connecting the centroids of the oldest mice to the centroids of the youngest mice visualizing the EpiAge axis.

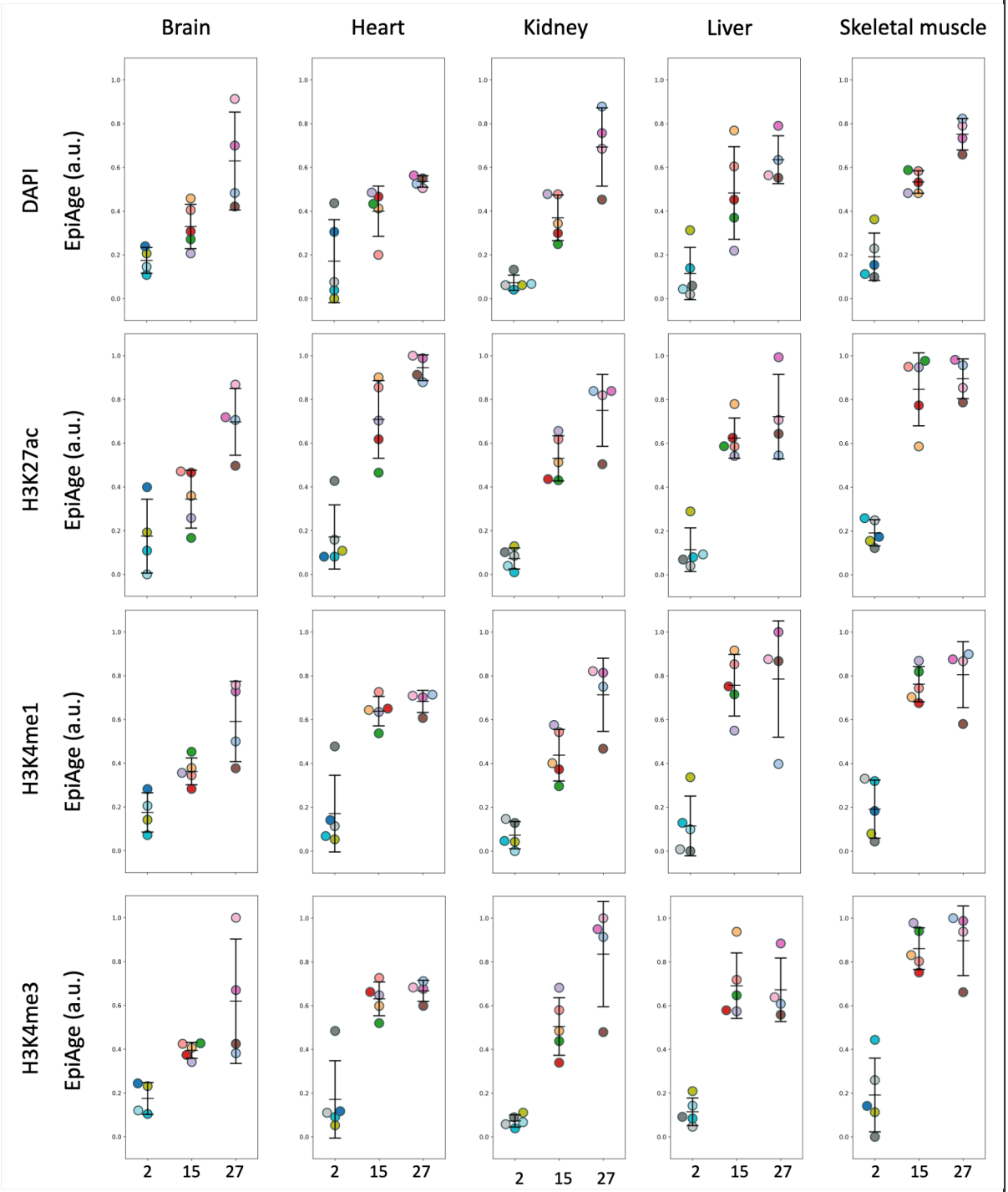

Supplementary Figure 3. Dot plot of EpiAge readouts from indicated organs and tissues. Y axis – normalized EpiAge (0-1) for each indicated epigenetic marks. Mice are color coded within each age group (young =2 months, mid-age =15 months, old=27 months).

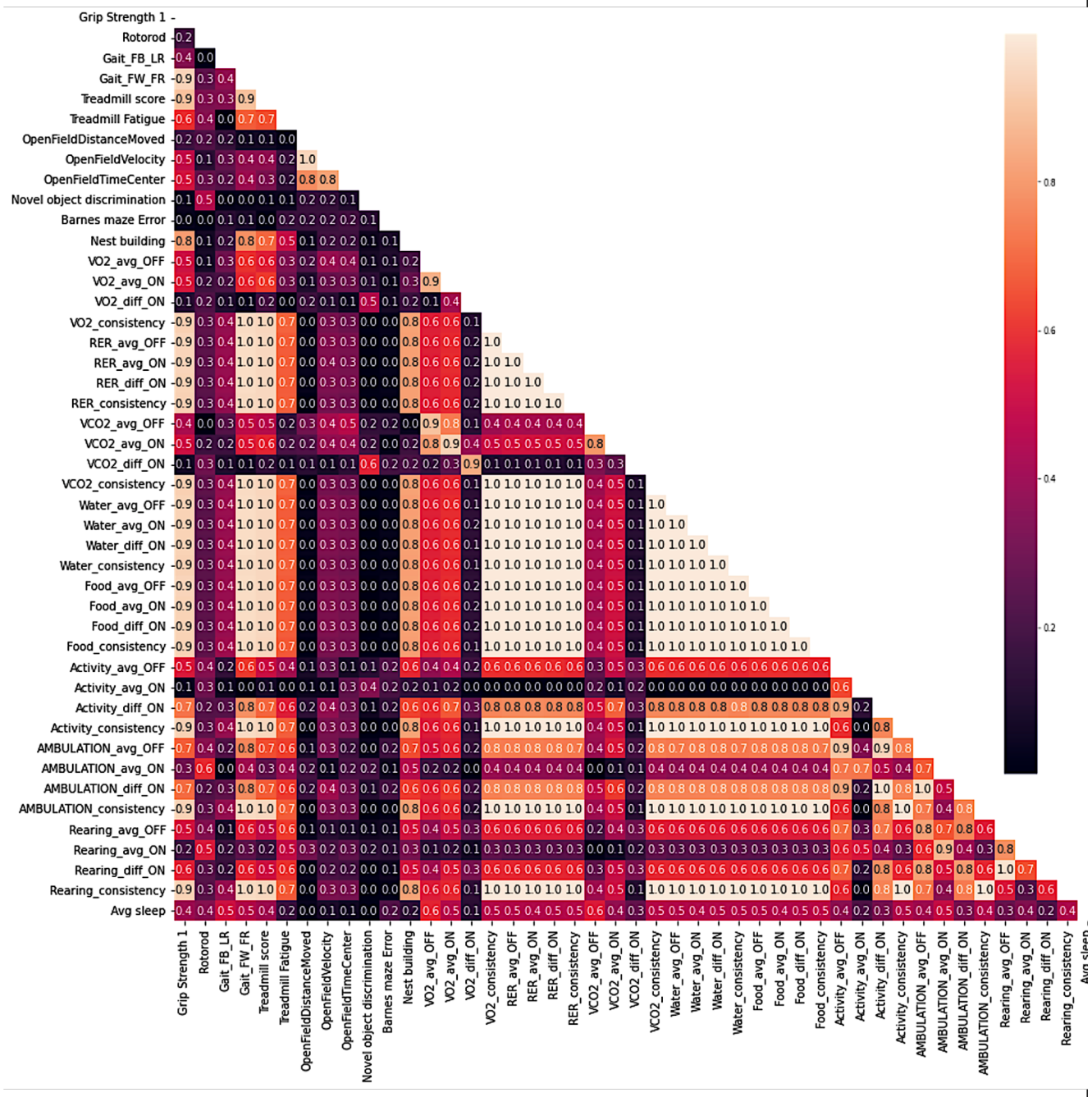

Supplementary Figure 4. Correlation matrix identifies co-linearity of metabolic and behavioral measurements. Since the CLAM includes measurements for the entire day. We have separated the features for light on and light off. Also, we have included the calculation of the average difference between the light off and light on. The correlation numbers have been rounded to 1 digit after the comma.

REFERENCES.

1. LaPierre, T.A. and M.E. Hughes, *Population aging in Canada and the United States*, in *International handbook of population aging*. 2009, Springer. p. 191-230.
2. Control, C.f.D. and Prevention, *Trends in aging--United States and worldwide.* MMWR. Morbidity and mortality weekly report, 2003. **52**(6): p. 101-106.
3. Jylhävä, J., N.L. Pedersen, and S. Hägg, *Biological age predictors.* EBioMedicine, 2017. **21**: p. 29-36.
4. Jones, J.A.B., et al., *The AgeGuess database, an open online resource on chronological and perceived ages of people aged 5–100.* Scientific Data, 2019. **6**(1): p. 1-8.
5. Simm, A., et al., *Potential biomarkers of ageing.* 2008.
6. Jazwinski, S.M. and S. Kim, *Examination of the Dimensions of Biological Age.* Front Genet, 2019. **10**: p. 263.
7. López-Otín, C., et al., *Hallmarks of aging: An expanding universe.* Cell, 2023.
8. Yang, J.-H., et al., *Loss of Epigenetic Information as a Cause of Mammalian Aging.* 2021.
9. Takahashi, K. and S. Yamanaka, *Induction of pluripotent stem cells from mouse embryonic and adult fibroblast cultures by defined factors.* Cell, 2006. **126**(4): p. 663-76.
10. Ocampo, A., et al., *In Vivo Amelioration of Age-Associated Hallmarks by Partial Reprogramming.* Cell, 2016. **167**(7): p. 1719-1733 e12.
11. Chondronasiou, D., et al., *Multi-omic rejuvenation of naturally aged tissues by a single cycle of transient reprogramming.* Aging Cell, 2022. **21**(3): p. e13578.
12. Tsurumi, A. and W. Li, *Global heterochromatin loss: a unifying theory of aging?* Epigenetics, 2012. **7**(7): p. 680-688.
13. Lee, J.-H., et al., *Heterochromatin: an epigenetic point of view in aging.* Experimental & Molecular Medicine, 2020. **52**(9): p. 1466-1474.
14. Villeponteau, B., *The heterochromatin loss model of aging.* Exp Gerontol, 1997. **32**(4-5): p. 383-94.
15. Tsurumi, A. and W.X. Li, *Global heterochromatin loss: a unifying theory of aging?* Epigenetics, 2012. **7**(7): p. 680-8.
16. Sen, P., et al., *Epigenetic Mechanisms of Longevity and Aging.* Cell, 2016. **166**(4): p. 822-39.
17. Lehnertz, B., et al., *Suv39h-mediated histone H3 lysine 9 methylation directs DNA methylation to major satellite repeats at pericentric heterochromatin.* Curr Biol, 2003. **13**(14): p. 1192-200.
18. Wang, Z., et al., *Combinatorial patterns of histone acetylations and methylations in the human genome.* Nat Genet, 2008. **40**(7): p. 897-903.
19. Boyer, L.A., et al., *Polycomb complexes repress developmental regulators in murine embryonic stem cells.* Nature, 2006. **441**(7091): p. 349-53.
20. van Kruijsbergen, I., et al., *Heterochromatic histone modifications at transposons in Xenopus tropicalis embryos.* Dev Biol, 2017. **426**(2): p. 460-471.
21. Nelson, D.M., et al., *Mapping H4K20me3 onto the chromatin landscape of senescent cells indicates a function in control of cell senescence and tumor suppression through preservation of genetic and epigenetic stability.* Genome Biol, 2016. **17**(1): p. 158.
22. Greer, E.L., et al., *Members of the H3K4 trimethylation complex regulate lifespan in a germline-dependent manner in C. elegans.* Nature, 2010. **466**(7304): p. 383-387.
23. Creyghton, M.P., et al., *Histone H3K27ac separates active from poised enhancers and predicts developmental state.* Proc Natl Acad Sci U S A, 2010. **107**(50): p. 21931-6.
24. Ucar, D., et al., *The chromatin accessibility signature of human immune aging stems from CD8(+) T cells.* J Exp Med, 2017. **214**(10): p. 3123-3144.

25. Maybury-Lewis, S.Y., et al., *Changing and stable chromatin accessibility supports transcriptional overhaul during neural stem cell activation and is altered with age.* Aging Cell, 2021. **20**(11): p. e13499.
26. Hannum, G., et al., *Genome-wide methylation profiles reveal quantitative views of human aging rates.* Mol Cell, 2013. **49**(2): p. 359-67.
27. Horvath, S., *DNA methylation age of human tissues and cell types.* Genome Biol, 2013. **14**(10): p. R115.
28. Lowe, R., et al., *Ageing-associated DNA methylation dynamics are a molecular readout of lifespan variation among mammalian species.* Genome Biol, 2018. **19**(1): p. 22.
29. Galow, A.M. and S. Peleg, *How to Slow down the Ticking Clock: Age-Associated Epigenetic Alterations and Related Interventions to Extend Life Span.* Cells, 2022. **11**(3).
30. Lu, A.T., et al., *DNA methylation GrimAge strongly predicts lifespan and healthspan.* Aging (Albany NY), 2019. **11**(2): p. 303-327.
31. Weidner, C.I., et al., *Aging of blood can be tracked by DNA methylation changes at just three CpG sites.* Genome Biol, 2014. **15**(2): p. R24.
32. Galkin, F., et al., *DeepMAge: A Methylation Aging Clock Developed with Deep Learning.* Aging Dis, 2020.
33. Bell, C.G., et al., *DNA methylation aging clocks: challenges and recommendations.* Genome Biol, 2019. **20**(1): p. 249.
34. Field, A.E., et al., *DNA Methylation Clocks in Aging: Categories, Causes, and Consequences.* Molecular Cell, 2018. **71**: p. 882-895.
35. Levine, M.E., et al., *An epigenetic biomarker of aging for lifespan and healthspan.* Aging (Albany NY), 2018. **10**(4): p. 573-591.
36. Zhang, Q., et al., *Improved precision of epigenetic clock estimates across tissues and its implication for biological ageing.* Genome Med, 2019. **11**(1): p. 54.
37. Farhy, C., et al., *Improving drug discovery using image-based multiparametric analysis of the epigenetic landscape.* Elife, 2019. **8**.
38. Severgnini, M., et al., *A rapid two-step method for isolation of functional primary mouse hepatocytes: cell characterization and asialoglycoprotein receptor based assay development.* Cytotechnology, 2012. **64**(2): p. 187-95.
39. Zhou, Y. and T.O. Sharpee, *Using global t-SNE to preserve inter-cluster data structure.* bioarxiv, 2018.
40. Zhou, Y. and T.O. Sharpee, *Hyperbolic geometry of gene expression.* iScience, 2021. **24**(3): p. 102225.
41. Zhou, Y., B.H. Smith, and T.O. Sharpee, *Hyperbolic geometry of the olfactory space.* Sci Adv, 2018. **4**(8): p. eaaq1458.
42. Praturu, A. and T. Sharpee, *A Bayesian Approach to Hyperbolic Embeddings.* Bulletin of the American Physical Society, 2022.
43. Piening, B.D., J. Lovejoy, and J.C. Earls, *Ageotypes: Distinct Biomolecular Trajectories in Human Aging.* Trends in pharmacological sciences, 2020. **41**(5): p. 299-301.
44. Ahadi, S., et al., *Personal aging markers and ageotypes revealed by deep longitudinal profiling.* Nat Med, 2020. **26**(1): p. 83-90.
45. Liu, Z., et al., *Underlying features of epigenetic aging clocks in vivo and in vitro.* Aging Cell, 2020. **19**(10): p. e13229.
46. Levine, M.E., et al., *An epigenetic biomarker of aging for lifespan and healthspan.* Aging (Albany NY), 2018. **10**(4): p. 573.

47. Sawada, M. and J.C. Carlson, *Changes in superoxide radical and lipid peroxide formation in the brain, heart and liver during the lifetime of the rat.* Mechanisms of ageing and development, 1987. **41**(1-2): p. 125-137.
48. Sanz, A., A. Bartke, and G. Barja, *Long-lived Ames dwarf mice: oxidative damage to mitochondrial DNA in heart and brain.* Journal of the American Aging Association, 2002. **25**(3): p. 119-122.
49. Jefferson, A.L., et al., *Cardiac index is associated with brain aging: the Framingham Heart Study.* Circulation, 2010. **122**(7): p. 690-697.
50. Demaria, M., et al., *Cellular Senescence Promotes Adverse Effects of Chemotherapy and Cancer Relapse.* Cancer Discov, 2017. **7**(2): p. 165-176.
51. Baar, M.P., et al., *Targeted Apoptosis of Senescent Cells Restores Tissue Homeostasis in Response to Chemotoxicity and Aging.* Cell, 2017. **169**(1): p. 132-147 e16.
52. Cupit-Link, M.C., et al., *Biology of premature ageing in survivors of cancer.* ESMO Open, 2017. **2**(5): p. e000250.
53. Hill, A., et al., *How cancer therapeutics cause accelerated aging: Insights from the hallmarks of aging.* J Geriatr Oncol, 2020. **11**(2): p. 191-193.
54. Madeo, F., et al., *Caloric Restriction Mimetics against Age-Associated Disease: Targets, Mechanisms, and Therapeutic Potential.* Cell Metab, 2019. **29**(3): p. 592-610.
55. Ma, S. and V.N. Gladyshev, *Molecular signatures of longevity: Insights from cross-species comparative studies.* Semin Cell Dev Biol, 2017. **70**: p. 190-203.
56. Balasubramanian, P., P.R. Howell, and R.M. Anderson, *Aging and Caloric Restriction Research: A Biological Perspective With Translational Potential.* EBioMedicine, 2017. **21**: p. 37-44.
57. Lacar, B., et al., *Nuclear RNA-seq of single neurons reveals molecular signatures of activation.* Nat Commun, 2016. **7**: p. 11022.
58. Baskin, K.K., B.R. Winders, and E.N. Olson, *Muscle as a "mediator" of systemic metabolism.* Cell metabolism, 2015. **21**(2): p. 237-248.
59. Meilă, M., *Comparing clusterings by the variation of information*, in *Learning theory and kernel machines*. 2003, Springer. p. 173-187.
60. Ganea, O., G. Becigneul, and T. Hofmann. *Hyperbolic neural networks*. in *Neurips*. 2018.
61. Zhavoronkov, A., et al., *Artificial intelligence for aging and longevity research: Recent advances and perspectives.* Ageing research reviews, 2019. **49**: p. 49-66.
62. Zhavoronkov, A., et al., *PsychoAge and SubjAge: development of deep markers of psychological and subjective age using artificial intelligence.* Aging (Albany NY), 2020. **12**(23): p. 23548.
63. Cole, J.H., et al., *Brain age and other bodily 'ages': implications for neuropsychiatry.* Molecular psychiatry, 2019. **24**(2): p. 266-281.
64. Nie, C., et al., *Distinct biological ages of organs and systems identified from a multi-omics study.* Cell Rep, 2022. **38**(10): p. 110459.
65. Cevenini, E., et al., *Human models of aging and longevity.* Expert Opin Biol Ther, 2008. **8**(9): p. 1393-405.
66. Kreienkamp, R., et al., *A Cell-Intrinsic Interferon-like Response Links Replication Stress to Cellular Aging Caused by Progerin.* Cell Rep, 2018. **22**(8): p. 2006-2015.
67. Schaum, N., et al., *Ageing hallmarks exhibit organ-specific temporal signatures.* Nature, 2020. **583**(7817): p. 596-602.
68. Carter, T.A., et al., *Mechanisms of aging in senescence-accelerated mice.* Genome Biol, 2005. **6**(6): p. R48.
69. Johnson, A.A., et al., *The role of DNA methylation in aging, rejuvenation, and age-related disease.* Rejuvenation Res, 2012. **15**(5): p. 483-94.

70. Nyce, J., *Drug-induced DNA hypermethylation and drug resistance in human tumors.* Cancer Res, 1989. **49**(21): p. 5829-36.
71. Sun, L., H. Zhang, and P. Gao, *Metabolic reprogramming and epigenetic modifications on the path to cancer.* Protein Cell, 2022. **13**(12): p. 877-919.
72. Ellis, L., P.W. Atadja, and R.W. Johnstone, *Epigenetics in cancer: targeting chromatin modifications.* Mol Cancer Ther, 2009. **8**(6): p. 1409-20.
73. Herranz, M. and M. Esteller, *DNA methylation and histone modifications in patients with cancer: potential prognostic and therapeutic targets.* Methods Mol Biol, 2007. **361**: p. 25-62.
74. Schumacher, B., G.A. Garinis, and J.H. Hoeijmakers, *Age to survive: DNA damage and aging.* Trends Genet, 2008. **24**(2): p. 77-85.
75. Hoeijmakers, J.H., *DNA damage, aging, and cancer.* New England Journal of Medicine, 2009. **361**(15): p. 1475-1485.
76. Bohr, V.A. and R.M. Anson, *DNA damage, mutation and fine structure DNA repair in aging.* Mutat Res, 1995. **338**(1-6): p. 25-34.
77. Wang, S., et al., *Cancer Treatment-Induced Accelerated Aging in Cancer Survivors: Biology and Assessment.* Cancers (Basel), 2021. **13**(3).
78. Shafqat, S., et al., *The Achilles' heel of cancer survivors: fundamentals of accelerated cellular senescence.* J Clin Invest, 2022. **132**(13).
79. Guida, J.L., et al., *Measuring Aging and Identifying Aging Phenotypes in Cancer Survivors.* J Natl Cancer Inst, 2019. **111**(12): p. 1245-1254.
80. Olsen, J.H., et al., *Lifelong cancer incidence in 47,697 patients treated for childhood cancer in the Nordic countries.* J Natl Cancer Inst, 2009. **101**(11): p. 806-13.
81. Rebholz, C.E., et al., *Health care use of long-term survivors of childhood cancer: the British Childhood Cancer Survivor Study.* J Clin Oncol, 2011. **29**(31): p. 4181-8.
82. Soto-Perez-de-Celis, E., et al., *Functional versus chronological age: geriatric assessments to guide decision making in older patients with cancer.* Lancet Oncol, 2018. **19**(6): p. e305-e316.
83. Bhakta, N., et al., *Cumulative burden of cardiovascular morbidity in paediatric, adolescent, and young adult survivors of Hodgkin's lymphoma: an analysis from the St Jude Lifetime Cohort Study.* Lancet Oncol, 2016. **17**(9): p. 1325-34.
84. Bullard, B.M., et al., *Nonpharmacological approaches for improving gut resilience to chemotherapy.* Current Opinion in Supportive and Palliative Care, 2022. **16**(3): p. 151-160.
85. Liao, C.Y., et al., *Genetic variation in the murine lifespan response to dietary restriction: from life extension to life shortening.* Aging Cell, 2010. **9**(1): p. 92-5.
86. Harper, J.M., C.W. Leathers, and S.N. Austad, *Does caloric restriction extend life in wild mice?* Aging Cell, 2006. **5**(6): p. 441-9.
87. Heilbronn, L.K. and E. Ravussin, *Calorie restriction and aging: review of the literature and implications for studies in humans.* Am J Clin Nutr, 2003. **78**(3): p. 361-9.
88. Al-Regaiey, K.A., *The effects of calorie restriction on aging: a brief review.* Eur Rev Med Pharmacol Sci, 2016. **20**(11): p. 2468-73.
89. Liang, Y., et al., *Calorie restriction is the most reasonable anti-ageing intervention: a meta-analysis of survival curves.* Sci Rep, 2018. **8**(1): p. 5779.
90. Hofman, M.A., *The human circadian clock and aging.* Chronobiology international, 2000. **17**(3): p. 245-259.
91. Chen, C.-Y., et al., *Effects of aging on circadian patterns of gene expression in the human prefrontal cortex.* Proceedings of the National Academy of Sciences, 2016. **113**(1): p. 206-211.
92. Mattis, J. and A. Sehgal, *Circadian rhythms, sleep, and disorders of aging.* Trends in Endocrinology & Metabolism, 2016. **27**(4): p. 192-203.

93. Van Someren, E.J., *Circadian rhythms and sleep in human aging.* Chronobiology international, 2000. **17**(3): p. 233-243.
94. Thompson, J.B., et al., *Sleep-length differences are associated with altered longevity in the fruit fly Drosophila melanogaster.* Biology open, 2020. **9**(9): p. bio054361.
95. Sabia, S., et al., *Association of sleep duration in middle and old age with incidence of dementia.* Nat Commun, 2021. **12**(1): p. 2289.
96. Lo, J.C., et al., *Sleep duration and age-related changes in brain structure and cognitive performance.* Sleep, 2014. **37**(7): p. 1171-8.
97. Kondratov, R.V., et al., *Early aging and age-related pathologies in mice deficient in BMAL1, the core componentof the circadian clock.* Genes & development, 2006. **20**(14): p. 1868-1873.
98. Krishnan, N., et al., *Loss of circadian clock accelerates aging in neurodegeneration-prone mutants.* Neurobiology of disease, 2012. **45**(3): p. 1129-1135.
99. Fonseca Costa, S.S. and J.A. Ripperger, *Impact of the circadian clock on the aging process.* Frontiers in neurology, 2015. **6**: p. 43.
100. Liu, F. and H.-C. Chang, *Physiological links of circadian clock and biological clock of aging.* Protein & cell, 2017. **8**(7): p. 477-488.
101. Jones, M.A. and M. Grotewiel, *Drosophila as a model for age-related impairment in locomotor and other behaviors.* Experimental gerontology, 2011. **46**(5): p. 320-325.
102. Ridgel, A.L. and R.E. Ritzmann, *Insights into age-related locomotor declines from studies of insects.* Ageing research reviews, 2005. **4**(1): p. 23-39.
103. Jucker, M., R. Oettinger, and K. Battig, *Age-related changes in working and reference memory performance and locomotor activity in the Wistar rat.* Behavioral and neural biology, 1988. **50**(1): p. 24-36.
104. Siwak, C.T., et al., *Age-dependent decline in locomotor activity in dogs is environment specific.* Physiology & behavior, 2002. **75**(1-2): p. 65-70.
105. Moscrip, T.D., et al., *Locomotor activity in female rhesus monkeys: assessment of age and calorie restriction effects.* The journals of gerontology series A: biological sciences and medical sciences, 2000. **55**(8): p. B373-B380.
106. Sallis, J.F., *Age-related decline in physical activity: a synthesis of human and animal studies.* Medicine & Science in Sports & Exercise, 2000. **32**(9): p. 1598-1600.
107. Volkow, N.D., et al., *Association between decline in brain dopamine activity with age and cognitive and motor impairment in healthy individuals.* American Journal of psychiatry, 1998. **155**(3): p. 344-349.
108. Sturman, O., P.-L. Germain, and J. Bohacek, *Exploratory rearing: a context-and stress-sensitive behavior recorded in the open-field test.* Stress, 2018. **21**(5): p. 443-452.
109. Lever, C., S. Burton, and J. O'Keefe, *Rearing on hind legs, environmental novelty, and the hippocampal formation.* Reviews in the Neurosciences, 2006. **17**(1-2): p. 111-134.
110. Walsh, R.N. and R.A. Cummins, *The open-field test: a critical review.* Psychological bulletin, 1976. **83**(3): p. 482.
111. Hollais, A.W., et al., *Effects of acute and long-term typical or atypical neuroleptics on morphine-induced behavioural effects in mice.* Clinical and Experimental Pharmacology and Physiology, 2014. **41**(3): p. 255-263.
112. Schefer, V. and M.I. Talan, *Oxygen consumption in adult and AGED C57BL/6J mice during acute treadmill exercise of different intensity.* Experimental gerontology, 1996. **31**(3): p. 387-392.
113. Hofmann, J.W., et al., *Reduced expression of MYC increases longevity and enhances healthspan.* Cell, 2015. **160**(3): p. 477-488.
114. Erema, V.V., et al., *Biological Age Predictors: The Status Quo and Future Trends.* International Journal of Molecular Sciences, 2022. **23**(23): p. 15103.

115. Oberdoerffer, P. and D.A. Sinclair, *The role of nuclear architecture in genomic instability and ageing.* Nature reviews Molecular cell biology, 2007. **8**(9): p. 692-702.
116. Oberdoerffer, P., et al., *SIRT1 redistribution on chromatin promotes genomic stability but alters gene expression during aging.* Cell, 2008. **135**(5): p. 907-918.
117. Marioni, R.E., et al., *The epigenetic clock is correlated with physical and cognitive fitness in the Lothian Birth Cohort 1936.* International journal of epidemiology, 2015. **44**(4): p. 1388-1396.
118. Levine, M.E., et al., *Epigenetic age of the pre-frontal cortex is associated with neuritic plaques, amyloid load, and Alzheimer's disease related cognitive functioning.* Aging (Albany NY), 2015. **7**(12): p. 1198.
119. Tinsley, F.C., G.Z. Taicher, and M.L. Heiman, *Evaluation of a quantitative magnetic resonance method for mouse whole body composition analysis.* Obesity research, 2004. **12**(1): p. 150-160.
120. Taicher, G.Z., et al., *Quantitative magnetic resonance (QMR) method for bone and whole-body-composition analysis.* Analytical and bioanalytical chemistry, 2003. **377**(6): p. 990-1002.
121. Champy, M.F., et al., *Exploration of metabolic and endocrine function in the mouse.* Standards of mouse model phenotyping, 2006: p. 109-133.
122. Yang, G., et al., *Central role of ceramide biosynthesis in body weight regulation, energy metabolism, and the metabolic syndrome.* American Journal of Physiology-Endocrinology and Metabolism, 2009. **297**(1): p. E211-E224.
123. Chang, Y., et al., *Ablation of NG2 proteoglycan leads to deficits in brown fat function and to adult onset obesity.* PLoS One, 2012. **7**(1): p. e30637.
124. Crawley, J.N., *Behavioral phenotyping of transgenic and knockout mice: experimental design and evaluation of general health, sensory functions, motor abilities, and specific behavioral tests.* Brain Res, 1999. **835**(1): p. 18-26.
125. Johnson, S.A., N.M. Fournier, and L.E. Kalynchuk, *Effect of different doses of corticosterone on depression-like behavior and HPA axis responses to a novel stressor.* Behavioural brain research, 2006. **168**(2): p. 280-288.
126. Winters, B.D., et al., *Double dissociation between the effects of peri-postrhinal cortex and hippocampal lesions on tests of object recognition and spatial memory: heterogeneity of function within the temporal lobe.* J Neurosci, 2004. **24**(26): p. 5901-8.
127. Mumby, D.G., et al., *Hippocampal damage and anterograde object-recognition in rats after long retention intervals.* Hippocampus, 2005. **15**(8): p. 1050-1056.
128. Berlyne, D.E., *Novelty and curiosity as determinants of exploratory behaviour.* British journal of psychology, 1950. **41**(1): p. 68.
129. Ennaceur, A. and J. Delacour, *A new one-trial test for neurobiological studies of memory in rats. 1: Behavioral data.* Behavioural brain research, 1988. **31**(1): p. 47-59.
130. Heyser, C.J. and A. Chemero, *Novel object exploration in mice: not all objects are created equal.* Behavioural processes, 2012. **89**(3): p. 232-238.
131. Crawley, J.N. and R. Paylor, *A proposed test battery and constellations of specific behavioral paradigms to investigate the behavioral phenotypes of transgenic and knockout mice.* Hormones and behavior, 1997. **31**(3): p. 197-211.
132. Carter, R.J., J. Morton, and S.B. Dunnett, *Motor coordination and balance in rodents.* Current protocols in neuroscience, 2001. **15**(1): p. 8.12. 1-8.12. 14.
133. Holmes, A., et al., *Behavioral profiles of inbred strains on novel olfactory, spatial and emotional tests for reference memory in mice.* Genes, Brain and Behavior, 2002. **1**(1): p. 55-69.
134. Bach, M.E., et al., *Impairment of spatial but not contextual memory in CaMKII mutant mice with a selective loss of hippocampal LTP in the range of the θ frequency.* Cell, 1995. **81**(6): p. 905-915.

135. Barnes, C.A., *Memory deficits associated with senescence: a neurophysiological and behavioral study in the rat.* J Comp Physiol Psychol, 1979. **93**(1): p. 74-104.
136. Paylor, R., et al., *Learning impairments and motor dysfunctions in adult Lhx5-deficient mice displaying hippocampal disorganization.* Physiology & behavior, 2001. **73**(5): p. 781-792.
137. Freitag, S., M. Schachner, and F. Morellini, *Behavioral alterations in mice deficient for the extracellular matrix glycoprotein tenascin-R.* Behavioural brain research, 2003. **145**(1-2): p. 189-207.
138. Crawley, J.N., *What's wrong with my mouse?: behavioral phenotyping of transgenic and knockout mice.* 2007: John Wiley & Sons.
139. Castro, B. and S. Kuang, *Evaluation of muscle performance in mice by treadmill exhaustion test and whole-limb grip strength assay.* Bio-protocol, 2017. **7**(8).
140. Mager, S.R., et al., *Standard operating procedure for the collection of fresh frozen tissue samples.* Eur J Cancer, 2007. **43**(5): p. 828-34.
141. Naber, S.P., *Continuing role of a frozen-tissue bank in molecular pathology.* Diagn Mol Pathol, 1996. **5**(4): p. 253-9.
142. Shabihkhani, M., et al., *The procurement, storage, and quality assurance of frozen blood and tissue biospecimens in pathology, biorepository, and biobank settings.* Clin Biochem, 2014. **47**(4-5): p. 258-66.
143. Sharpee, T.O., *An argument for hyperbolic geometry in neural circuits.* Current opinion in neurobiology, 2019. **58**: p. 101-104.
144. Verleysen, M. and D. François. *The curse of dimensionality in data mining and time series prediction.* in *International work-conference on artificial neural networks.* 2005. Springer.
145. Kuo, F.Y. and I.H. Sloan, *Lifting the curse of dimensionality.* Notices of the AMS, 2005. **52**(11): p. 1320-1328.
146. Bellman, R., *Dynamic programming, 1957.* A very comprehensive reference with many economic examples is, 2003.